GC_SRF: A new generalized strategy for obtaining the lithospheric thickness from S-wave receiver functions and its application to southeastern Tibet

Zhou Zhang[1,2,3], Yangfan Deng[1,2*]

[1]State Key Laboratory of Isotope Geochemistry, Guangzhou Institute of Geochemistry, Chinese Academy of Sciences, Guangzhou, China.

[2]CAS Center for Excellence in Deep Earth Science, Guangzhou, 510640, China.

[3]College of Earth and Planetary Sciences, University of Chinese Academy of Sciences, Beijing, China.

Corresponding author: Yangfan Deng (yangfandeng@gig.ac.cn)

Key Points:

- A new generalized strategy for obtaining the lithospheric thickness from S-wave receiver functions (GC_SRF) is proposed.
- This GC_SRF strategy can rebuild the Sp converted phase from either full wavefield synthetic seismograms or field data without artificats.
- Lateral variations in the lithospheric structure from the Sichuan Basin to Tengchong Volcano in southeastern Tibet are investigated.

Abstract

The selected rotation angle and deconvolution time window during S-wave receiver function (SRF) calculations and the final SRF quality control may introduce artificial interference. Here we overcome these problems by proposing a new strategy, the GC_SRF strategy, which employs grid search and correlation analysis to obtain reliable SRFs. Extensive tests using synthetic and real data suggest that the GC_SRF strategy is a suitable approach for constraining lithospheric thickness, and reproducible and robust depth estimations of the lithosphere–asthenosphere boundary (LAB) are obtained. Specifically, this GC_SRF strategy can restore the weak Sp phases from full wavefield synthetic seismograms. Similar, but clearer, discontinuity patterns that contain no artificial interference compared with those obtained in previous studies of southeastern Tibet are produced here. The post-stack migrated SRFs reveal that the Chuandian region has a thicker crust and either a poorly defined or unclear LAB, whereas a thinner crust and clear LAB is present at ~160 km depth beneath the Sichuan Basin. The absence of a continuous LAB in the Chuandian region may suggest lithospheric regrowth due to mantle plume processes.

Plain Language Summary

As the outermost shell of the solid Earth, the lithosphere attracts great attention because it can be considered a natural "archive" that records the evolutionary history of the Earth. In addition, it represents the Earth’s reservoir for mineral resources, and oil, and gas, and it is the origin of numerous natural disasters, such as volcanic eruptions and earthquakes. It is therefore essential to understand the spatial morphology of the lithosphere and its evolution. In this study, we introduce a new strategy, the GC_SRF strategy, to obtain the lithospheric thickness while avoiding any potential artificial interference based on the traditional S-wave receiver function technique. This newly developed strategy can obtain robust and clear lithospheric thicknesses from synthetic seismograms. We also analyze real data to image the lithospheric structure in southeastern Tibet based on this GC_SRF strategy, which provides consistent but clearer results compared with previous studies. This strategy can be applied to other complex geological environments to advance our understanding of geodynamic processes.

1. Introduction

The lithosphere–asthenosphere boundary (LAB) is generally considered to be a negative velocity gradient transition zone from the cold and fast lithosphere to the warm and slow asthenosphere. Its depth varies considerably, ranging from <50 km beneath the youngest ocean to >200 km beneath cratonic regions (Thybo, 2006; Fischer et al., 2010; Hopper & Fischer, 2015; Fischer et al., 2020). The precise positioning of the LAB provides good constraints on the evolution of cratons and orogens, such as lithospheric thinning owing to extension (Buck, 1991) and lithospheric thickening owing to collision (Houseman et al., 1981). A series of methods, such as receiver functions (P- and S-wave receiver functions; PRFs and SRFs, respectively), SS precursors, and body-wave and surface-wave tomography, have been developed to detect the lithospheric thickness at both global (Bijwaard & Spakman, 2000; Ritzwoller et al., 2002; Ritsema et al., 2004) and local scales (Rawlinson & Fishwick, 2012; Mojaver et al., 2021; Zhang et al., 2021).

SRFs are the most widely used method for detecting the LAB because the Sp converted phase is remarkably sensitive to the vertical velocity gradient across the LAB (Chen et al., 2009; Hansen et al., 2010; Hu et al., 2011; Zhang et al., 2014; Liu et al., 2021; Liu & Zhao, 2021; Thybo et al., 2021). Coordinate system rotation and deconvolution are important steps for obtaining SRFs. However, the incident angle of the planar S wave could be different from the synthetic value due to the complexity of the earthquake mechanisms and near-surface structures beneath the seismic stations. The deconvolution time window may also include mixtures of different seismic phases. Here, we identified the incidence angle (Inci_Ang) and window length (Win_Len) as the two key parameters in this study. We calculated the SRFs by varying these two parameters to mimic the three-component waveforms at station ST09 on the Tibetan Plateau, which has been analyzed in a previous study (Kumar et al., 2006). Figure 1 shows that different values of these two parameters can indeed affect the shape of the SRFs. The waveform amplitude at time zero could be either negative or positive for different Inci_Ang and Win_Len values. Furthermore, the quality control process of the estimated SRFs could also influence the stacking and migration results. Therefore, the inappropriate selection of the coordinate rotation angle and deconvolution time window, and following quality control process would potentially bias the resultant LAB depth.

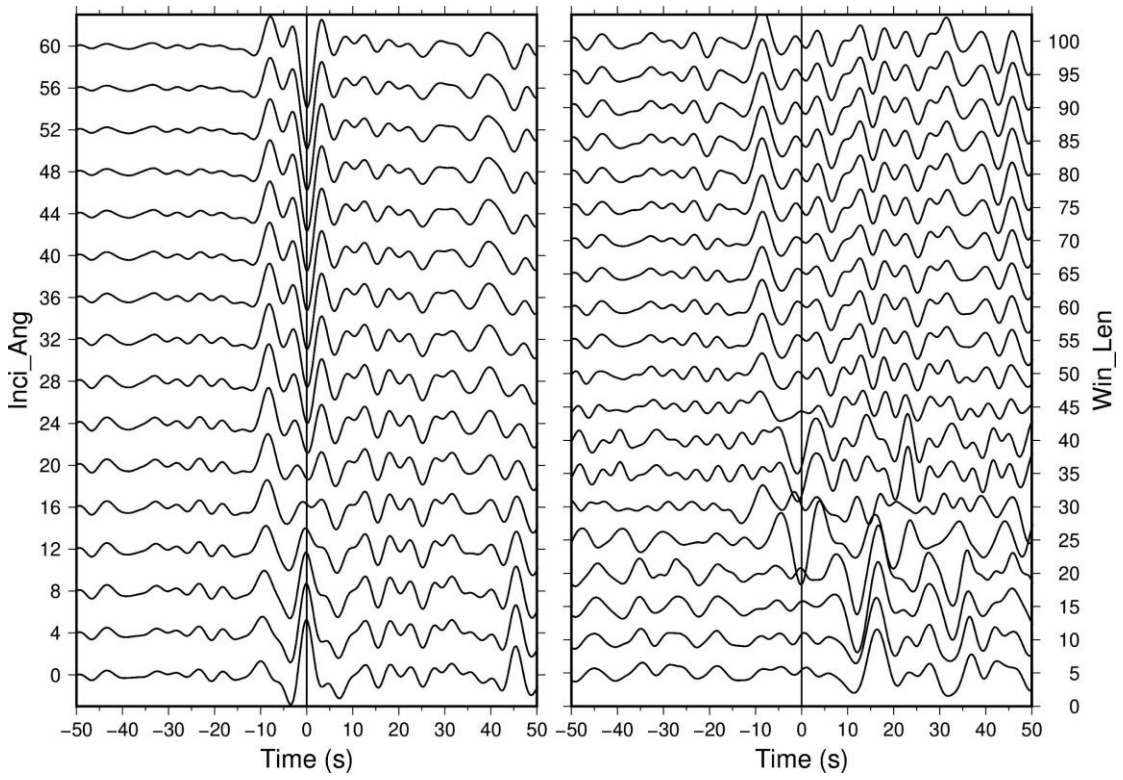

Figure 1. The influence of the incidence angle (Inci_Ang) and deconvolution time window length (Win_Len) on the shape of the S wave receiver function.

Various efforts have been made to optimize the coordinate rotation angle and quality control process to improve the reliability and stability of the constructed SRFs. Minimizing the amplitude at time zero (Kumar et al., 2006; Yuan et al., 2006; Kind et al., 2012; Zhang et al., 2012), measuring the polarization angle based on the S-wave particle motion (Farra & Vinnik, 2000; Vinnik et al., 2004), and converting from the apparent velocity (Reading et al., 2003; Hu et al., 2011) are all reliable approaches for determining the possible rotation angle. The quality control process includes visual inspection, signal-to-noise ratio (SNR) constraints (Hansen et al., 2010; Shen et al., 2019), and bootstrap estimation (Hansen et al., 2009; Xu et al., 2017; Xu et al., 2019). However, these methods could introduce artifacts based on the parameters chosen. A robust and repeatable strategy that avoids artificial interference when obtaining SRFs has not been implemented to date.

Here we focus on avoiding such artificial interference when obtaining the lithospheric thickness by varying Inci_Ang and Win_Len during the SRF calculation and then performing a quality control on the resultant SRFs. We develop the GC_SRF strategy to extract stable SRFs

and guarantee reproducibility, where the “G” and “C” represent the grid search and correlation analysis, respectively. Specifically, we first perform a grid search to obtain the two parameters, Inci_Ang and Win_Len. We then analyze the SRFs corresponding to different combinations of these two parameters via cross-correlation to obtain the optimal SRF. The root mean square error (RMSE) algorithm is introduced to perform the quality control process in real data cases. Parallel computing is introduced to ensure computational efficiency of the GC_SRF strategy. This strategy has been effectively applied to both full wavefield synthetic seismograms and real data sets collected in southeastern Tibet.

2. Method

The GC_SRF strategy is schematically illustrated in Figure 2. This approach contains coordinate rotation and discrete deconvolution (Farra & Vinnik, 2000; Wilson et al., 2006; Yuan et al., 2006) steps during the SRF calculation process. We follow the approach outlined in Kumar et al. (2006) and Yuan et al. (2006) to rotate the raw data from the ZNE system to the LQT system and determine the optimal Inci_Ang value by minimizing the amplitude at time zero on the L component.

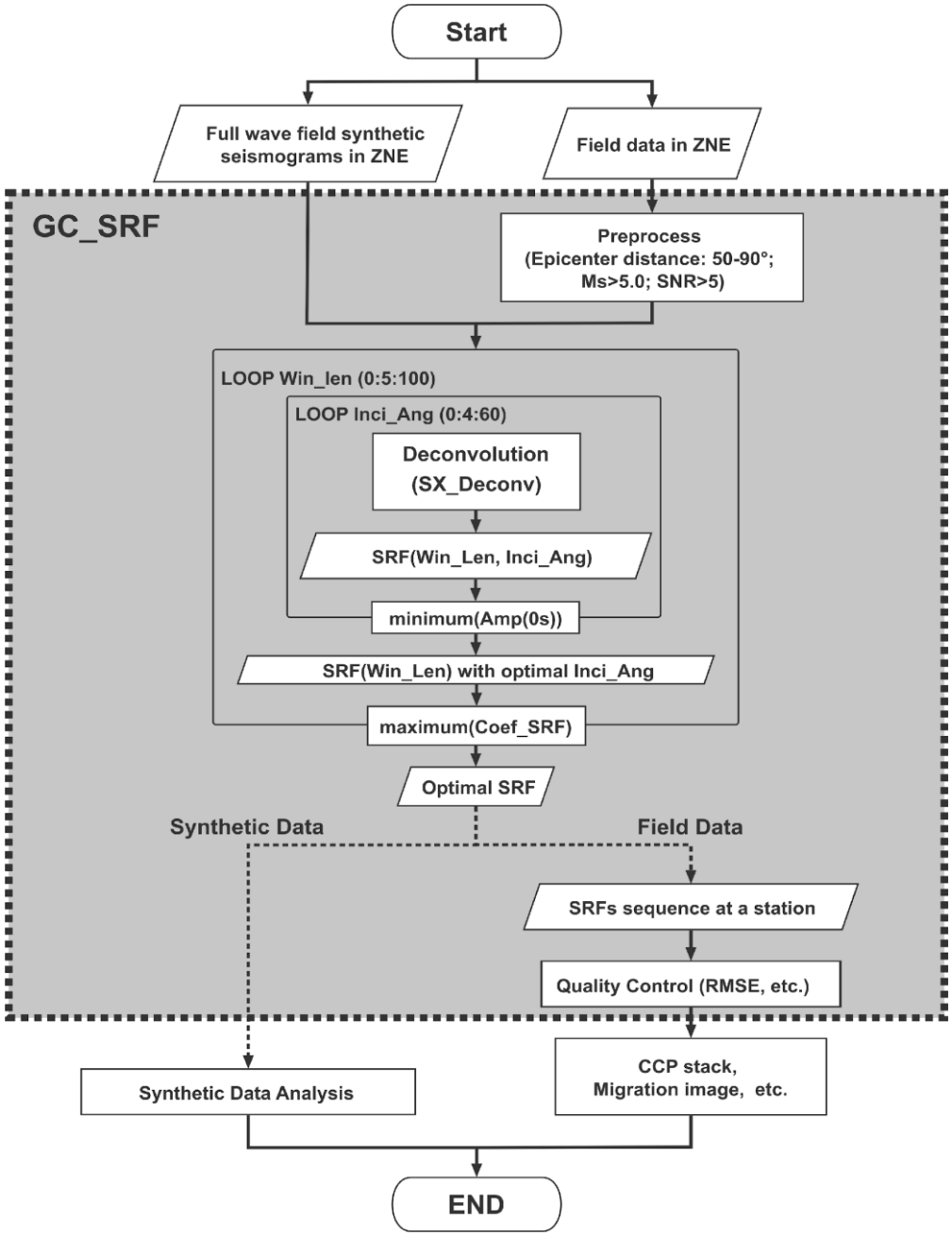

Figure 2: Flow chart of the GC_SRF strategy.

The concept of discrete deconvolution has been employed in reflection seismology since the 1950s (Robinson & Treitel, 2000), and it was later introduced in passive seismology, where it has since been developed into different algorithms, such as time-domain iterative deconvolution (Ligorria & Ammon, 1999), wiener filter deconvolution (Wu et al., 2003a), water level deconvolution (Langston, 1979), maximum entropy spectrum deconvolution (Wu et al., 2003b),

115 homomorphic deconvolution (Oppenheim, 1969; Ulrych et al., 1972), and spiking deconvolution
116 (Treitel & Robinson, 1966; Robinson & Treitel, 1976; 2000). We have chosen spiking
117 deconvolution in the GC_SRF strategy because of its wide use and efficiency in previous SRF
118 studies (Farra & Vinnik, 2000; Yuan et al., 2006; Kind et al., 2012). Spiking deconvolution is
119 employed in the LQT coordinate system to estimate an inverse filter based on a chosen time
120 window of the Q-component waveform (Levinson, 1946; Rost & Thomas, 2002). The length of
121 the time window (Win_Len) led directly to the instability of the deconvolution results (see
122 Figure 1).

123 The spiking deconvolution algorithm that is used in most studies is enclosed in the
124 Seismic Handler (Stammler, 1993), which is now inconvenient to use because it has not been
125 maintained for nearly a decade. We therefore reconstruct the spiking deconvolution algorithm as
126 a binary executable named SX_Deconv using the C++ compiler to handle and transplant the
127 algorithm for different applications. We reproduce the results presented in Kumar et al. (2006) to
128 validate the effectiveness of SX_Deconv. Figure 3 provides a comparison of the SRFs obtained
129 by two algorithms for a Ms 6.4 earthquake event in 1998 at station ST09, with the Kumar et al.
130 (2006) result shown in Figure 3a and the SX_Deconv result, where Inci_Ang varies from 0 to 60
131 and Win_Len is set to 85, as shown in Figure 3b.

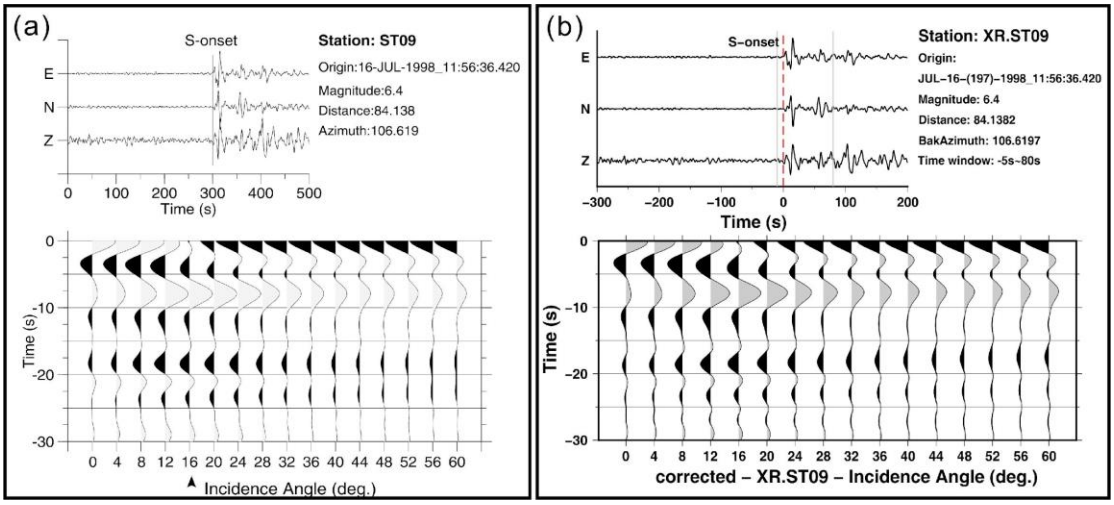

132

133 **Figure 3:** SRFs at station ST09 in southwestern Tibet with an Ms 6.4 earthquake event in 1998.
134 (a) An example edited from Figure 4b in Kumar et al 2006. (b) Result using SX_Deconv. The
135 top panel represents the original three-component event waveforms and event information. The

bottom panel shows the SRFs corresponding to different incidence angles with deconvolution time window length fixed to 85 s.

The upper panel in Figure 3 shows the original seismic event waveform and earthquake information, which indicates that the event waveform we collected from the Incorporated Research Institutions for Seismology (IRIS) is the same as that in Kumar et al. (2006). The lower panel of Figure 3 shows the calculated SRFs for different rotation angles, with identical SRFs on both sides that possess clear Sp phases, a positive Smp phase near –8 s, and a negative SLp phase near –18 s. These results validate the application of this algorithm to obtain SRFs from both synthetic and real data.

The three-component event waveforms that were recorded in the ZNE coordination system serve as the inputs for the GC_SRF strategy. We prepare the input data for the synthetic cases via the following procedure: (1) apply a 50- to 4-s bandpass filter; (2) clip the waveforms from 200 s before to 200 s after the theoretical S-wave arrival time, which was calculated using the IASP91 model (Kennett & Engdahl, 1991) and TauP Toolkit (Crotwell et al., 1999); and (3) detrend, demean, and resample the waveforms to 0.1 s. Similarly, the preparation steps for real data are: (1) select the teleseismic S waveforms for Ms ≥5.5 earthquakes with epicentral distances in the 50°–90° range that possess SNR_H greater than 5; (2) remove the instrument response using a 50- to 4-s bandpass filter; (3) clip the waveforms from 200 s before to 200 s after the theoretical S-wave arrival time; and (4) detrend, demean, and resample the waveforms to 0.1 s. Here we define the SNR_H as:

$$SNR_H = \frac{SNR_N + SNR_E}{2}, \qquad (1)$$

where SNR_N is the SNR of the N component and SNR_E is the SNR of the E component, with the signal window defined as 5 s before to 30 s after the S-wave arrival time and the noise window defined as 60 to 30 s before the S-wave arrival time.

The GC_SRF strategy calculates the SRFs corresponding to different Inci_Ang and Win_Len values (i.e., $SRF(Inci\_Ang, Win\_Len)$). Here, Inci_Ang is varied from 0° to 60° in 4° increments (Kumar et al., 2006), and Win_Len is varied from 5 s to 100 s in 5-s increments. There is only one SRF waveform for each Win_Len, with the smallest absolute amplitude

occurring at time zero ($SRF_{\min(Win\_Len)}$). The arithmetic mean of these SRFs is redefined as the reference SRF (SRF_{ref}):

$$SRF_{ref} = \frac{1}{N}\sum SRF_{\min(Win\_Len)}, \qquad (2)$$

where N indicates the number of Win_Len values. The cross-correlation coefficient between the SRF_{ref} and $SRF(Inci\_Ang, Win\_Len)$ is then defined as:

$$Coef_{SRF}(Inci\_Ang, Win\_Len) = CC[SRF_{ref},\ SRF(Inci\_Ang, Win\_Len)], \qquad (3)$$

where CC indicates the cross-correlation coefficient calculation. Finally, only the SRF that simultaneously satisfies (1) the smallest absolute amplitude at time zero and (2) the maximum $Coef_{SRF}$ will be selected as the optimal SRF. The Inci_Ang and Win_Len values corresponding to this optimal SRF can either be used as a reference waveform for quality control or as input parameters that can be adapted to other deconvolution methods.

It is still necessary to perform quality control on the estimated SRFs from real data to remove any ambient noise and aliased waveforms. The results for a single station should have good consistency, as has been fully demonstrated in previous receiver function studies (Kumar et al., 2006; Yuan et al., 2006), because the receiver function technique reflects the structural information below the station (Rost & Thomas, 2002; Kumar et al., 2010). Therefore, the RMSE is applied for the quality control step. We first calculate the RMSE between each SRF and the average waveform at each station. We then reorder all of the SRFs based on their RMSEs, with waveforms possessing clear and consistent Smp and SLp phases tending to be at the beginning of the sequence. We can select different proportions of the SRFs based on this reordered sequence to perform a linear summation. The best selection percentage can be determined by comparing the amplitudes of the Smp and SLp phases of the stacked waveforms that correspond to different data proportions. Here, we name this reordering method RMSE reordering and the best data proportion RMSE percentage.

3 Applications of the GC_SRF strategy to full wavefield synthetic seismograms

3.1 Application to a one-dimensional (1-D) velocity model

We first test the GC_SRF strategy on full wavefield synthetic seismograms using 1-D velocity models to demonstrate that this strategy can effectively calculate SRFs. Several attempts

have been made previously to obtain synthetic full wavefield seismograms and synthetic SRFs (Yuan et al., 2006; Shen et al., 2019). Yuan et al. (2006) synthesized full wavefield seismograms via the reflectivity method (QSEIS, (Wang, 1999)); however, they obtained SRFs with only partial wavefield synthetic seismograms to avoid the deconvolution calculation. Although the partial wavefield synthetic seismograms possessed clear Sp converted phases, the observed field data consist of time series signals from the full wavefield. It is therefore necessary to rebuild the Sp phases from full wavefield synthetic seismograms to ensure the robustness of our proposed strategy.

The 1-D models that are employed in this study, which are constructed to a depth of 1000 km based on IASP91 (Kennett & Engdahl, 1991), are shown in Figure 4, with the crust simplified to a single 40-km-thick layer. We introduce a 5% negative velocity jump at either 120 km (SM01), 150 km (SM02), or 180 km (SM03) depth to represent the LAB, following Yuan et al. (2006). We then employ the reflectivity method (Wang, 1999) to obtain full wavefield seismograms (Figure 5).

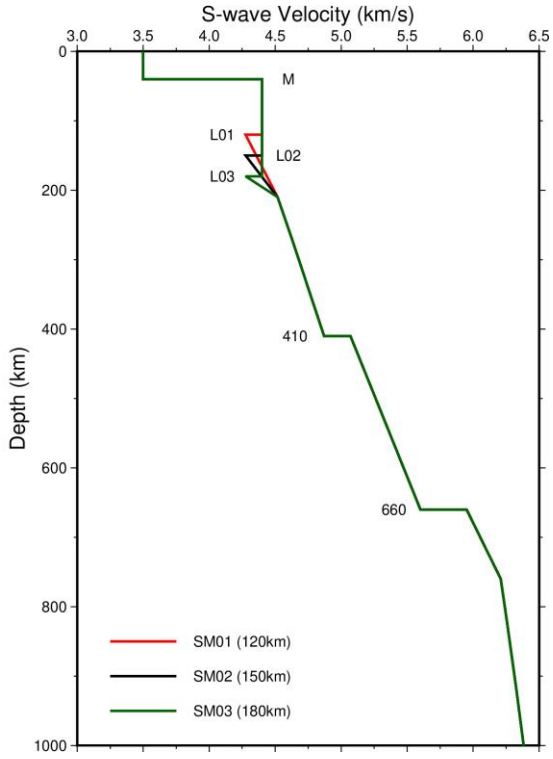

Figure 4: Models of S wave velocities for calculating the full wavefield synthetic seismograms. Three models SM01 (red), SM02 (black) and SM03 (dark green) are plotted in different colors.

Compared with the IASP91 model, we simplified the crust to a single 40 km thick layer and only showed the upper 1000 km of our models here.

The synthetic seismograms that correspond to the three models in Figure 4 are shown in Figure 5. The travel time curves of the SLp phase (which represents the seismic phase converted at the LAB) for the three models are plotted as dashed lines (MOD01: red, MOD02: black; MOD03: green). The dashed cyan lines represent the other theoretical phases from the SM02 model, whose LAB depth (150 km) is between those of the other two models. It is clear that the various Sp converted phases cannot be recognized easily from the full wavefield synthetic seismograms. The details of the various Sp phases (including Smp, S410p, ScS410p, ScS660p, SKS410p, and SKS660p) are difficult to identify on the N (Figure 5b) and Z (Figure 5a) components, as these phases are significantly weaker than either the ScS or SKS phases (Figure 5a). This is consistent with the full wave field synthetic seismogram shown in a previous study (Yuan et al., 2006), even though we use three modified velocity models in this study.

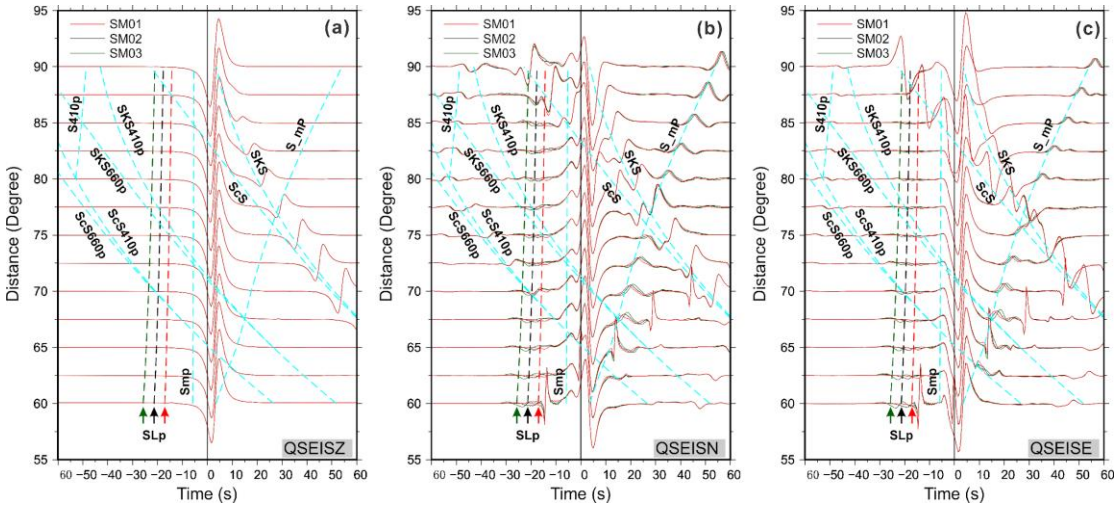

Figure 5. Vertical (a), North (b) and East (c) component full wavefield synthetic seismograms calculated by the reflectivity method (QSEIS, Wang, 1999) for the model shown in Figure. 4. Time axis is aligned by S arrival time. The main phases are labeled on the corresponding components.

We apply the GC_SRF strategy to the full wavefield synthetic seismograms and obtain SRFs for all of the Inci_Ang and Win_Len pairs. We present the GC_SRF results with an epicentral distance of 75° using model SM01 in Figure 6 to compare the differences among the three models (SM02: Figure S1; SM03: Figure S2). Figure 6a shows a color map of the

amplitudes at time zero on the L component (SRFL), whereas Figure 6b, 6g, and 6l show $Coef_{SRF}$ for all of the parameter pairs. The dashed black line in Figure 6a indicates the incident angles of the S phase that are calculated by the TauP Toolkit (Crotwell et al., 1999), and the green crosses represent the position with the lowest amplitude; here the optimal SRF for each Win_Len value is selected where there is a polarity change in the waveform. Figure 6b shows a color map of $Coef_{SRF}$, with the dashed line and green crosses representing the same variables as those in Figure 6a. The red crosses in these figures indicate the final optimal SRFs. The waveforms of all of the SRFs in Figure 6d are shown as solid gray curves, and the waveforms that correspond to the optimal SRFs for each Win_Len value are shown as solid green curves. We also show the $Coef_{SRF}$ corresponding to all of the green and red waveforms in Figure 6e. The red curves in Figure 6d and the red crosses in Figure 6e indicate the optimal SRF (with the max $Coef_{SRF}$). Examples for models SM02 and SM03 are shown in Figures S2 and S3, respectively.

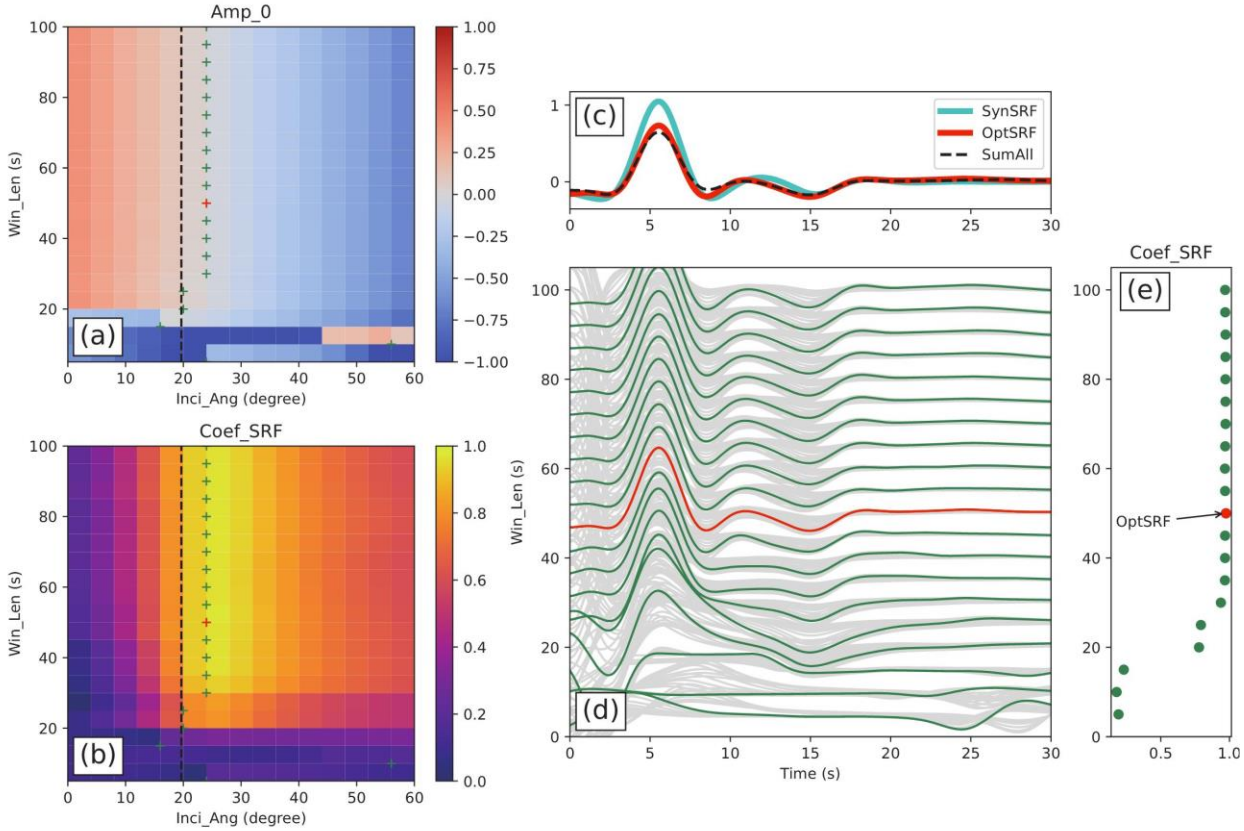

Figure 6: GC_SRF examples for SM01 ($t_S - t_{SLp} = 15.35s$) with an epicentral distance of 75°. (a) Color map of the amplitude at time zero of the L component. (b) color map of the $Coef_{SRF}$.

(c) Comparison of Synthetic SRF (cyan), linear stacked SRF (black dashed), and the optimal SRF from GC_SRF. (d) All the SRFs corresponding to different $Inci\_Ang$ and Win_Len pairs (green curves show the optimal SRF for each Win_Len, the red curve represents the final optimal SRF, and the gray curves show the other SRFs). (e) $Coef_{SRF}$ corresponding to all green and red crosses in (a) and (b).

To present the efficiency of our proposed GC_SRF strategy, we calculate the theoretical synthetic SRFs using the three models (cyan curves in Figure 6c) via the propagator matrix method (Haskell, 1962). This method is efficient in obtaining the P- and SV-wave responses of a horizontally isotropic layered medium, which is often compared with the observed SRF (Randall, 1989; Niu & Kawakatsu, 1996; Vinnik et al., 2001). The dashed black waveform in Figure 6c is the linear stack of the SRFs that correspond to all the parameter pairs, whereas the red waveform corresponds to the optimal SRF. The optimal SRFs are in good agreement with the theoretical synthetic SRFs for the different models (Figure 6c, and Figures S1c and S2c). These tests demonstrate the stability and reproducibility of the GC_SRF strategy. We then plot the optimal SRFs (SRFL) as a function of epicentral distance in Figure 7a.

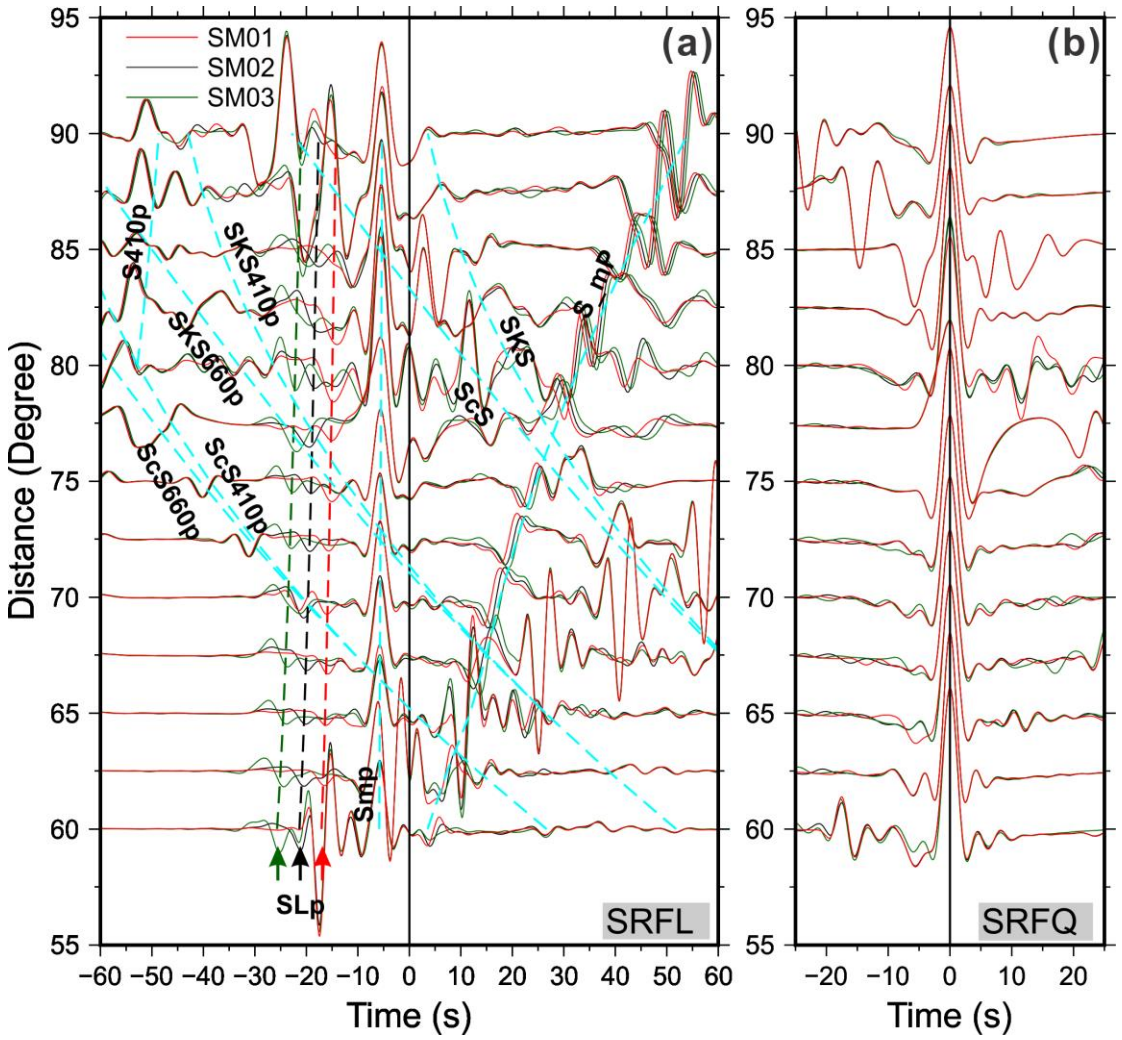

Figure 7: SRFs as a function of epicentral distances. The converted 'p' phases are labeled, including Smp, SLp, S410p, ScS410p, ScS660p, SKS410p, and SKS660p. (a) deconvolved L component (SRFL). (b) deconvolved Q component (SRFQ).

The synthetic tests for the 1-D velocity model indicate that the GC_SRF strategy can successfully recover the Sp converted phases (see Figure 7). Notably, the Q-component (SRFQ) plot in Figure 7c has been suggested to reflect information on the earthquake sources (Vinnik et al., 2004; Kawakatsu et al., 2009). It is also evident that the Smp seismic phase is highly consistent at 5 s for the three models, as they all possess the same crustal thickness. Other notable features are the significant time shifts in the SLp phases for the three models and the fit of the peaks of the SLp phases to the theoretical travel time (see Table 1) within a certain range of epicentral distances (60°–80°). Furthermore, the results demonstrate that many other Sp

phases, such as S410p, ScS410p, ScS660p, SKS410p, and SKS660p, can be rebuilt without artifacts.

Model name	Epicentral distances (degree)	t_{Smp}-t_S (s)	t_{SLp}-t_S (s)
SM01 Moho 40km LAB 120km	60	-5.85	-17.04
	65	-5.74	-16.35
	70	-5.64	-15.82
	75	-5.55	-15.35
	80	-5.47	-14.96
SM02 Moho 40km LAB 150km	60	-5.85	-21.34
	65	-5.74	-20.40
	70	-5.64	-19.68
	75	-5.55	-19.06
	80	-5.47	-18.54
SM03 Moho 40km LAB 180km	60	-5.85	-25.70
	65	-5.74	-24.47
	70	-5.64	-23.56
	75	-5.55	-22.79
	80	-5.47	-22.14

Table 1 The synthetic time residual of Smp to S and SLp to S. The waveforms with epicentral distance of 75° are shown in Figures 6, S1 and S2.

3.2 Application to a two-dimensional (2-D) velocity model and post-stack migration

The robustness of the imaged discontinuities needs to be further demonstrated to ensure that a reliable lithospheric thickness is obtained; we therefore perform a resolution test for the 2-

D case via forward modeling. We first construct a 2-D velocity model that is modified from IASP91 (Figure 8a) and calculate the full wavefield seismograms for a pseudo profile using 10 stations. The GC_SRF strategy is then used to calculate SRFs. A wave equation-based post-stack migration method (Chen et al., 2005a; b) is employed for this resolution test. The moveout-corrected SRFs are first processed using time-domain common conversion-point (CCP) stacking, and the stacked SRFs are subsequently processed using frequency-domain backward wavefield extrapolation to obtain the migrated images (Chen, 2009; Chen et al., 2009). We use rectangular stacking bins when performing CCP stacking. The bin width, which is perpendicular to the profile, is set to 200 km, whereas the bin length, which parallels the profile, varies with depth and data coverage. The modeling results (Figure 8b) show that the interface morphology in the theoretical velocity model can be recovered by migrating the SRF obtained by the GC_SRF strategy. The resolution test also indicates that the GC_SRF strategy is capable of obtaining reliable SRFs without artificial interference.

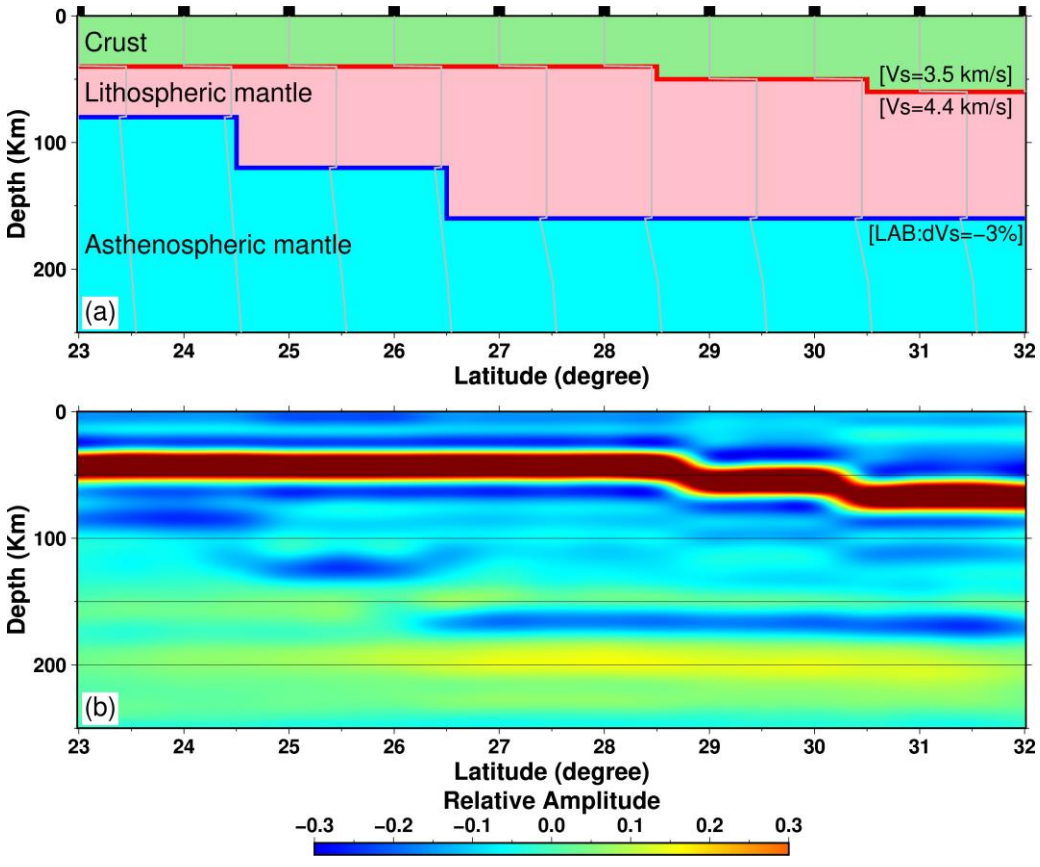

Figure 8: Synthetic test for 2-D velocity model. (a) Synthetic velocity model modified from IASP91. The black boxes on the frame show the pseudo stations where the 1-D velocity curves

296 are plotted in gray. The red line indicates the Moho discontinuity, and the blue line represents the
297 LAB discontinuity. Velocity changes at discontinuities are labeled. (b) Post-stack migrated
298 image of the GC_SRF results. The cutoff frequency limit is set to be 0.05-0.25Hz.

299 **4 Application to stations in southeastern Tibet**

300 It is necessary to test this strategy in a given region to validate its applicability and
301 feasibility in LAB detection. Here we apply the GC_SRF strategy to seismic stations in
302 southeastern Tibet, a collision area between the Eurasian and Indian plates. This area is adjacent
303 to the Sichuan Basin in the east, and spans the Tengchong Volcano region and Permian
304 Emeishan Large Igneous Province. Furthermore, this area is widely believed to possess channels
305 that promote the eastward escape of materials from the Qinghai-Tibet Plateau (Molnar &
306 Tapponnier, 1975; Tapponnier et al., 1982). Several large-scale geophysical investigations have
307 previously been conducted across this region, including surface-wave tomography (e.g., Yao et
308 al., 2008; Huang et al., 2013; Yao, 2020), body-wave tomography (e.g., Lei et al., 2014; Lei &
309 Zhao, 2016), and PRF imaging (e.g., Xu et al., 2013; Ye et al., 2017).

310 Recent Rayleigh-wave tomographic results have shown that a high-velocity pattern is
311 present at the LAB depth under the Chuandian region (Fu et al., 2017), whereas a body-wave
312 tomographic study (Huang et al., 2019) has revealed a low-velocity pattern at the same depth
313 range. Deng et al. (2021) obtained an independent constraint on the architecture via body-wave
314 attenuation tomography, which suggested that the Sichuan Basin and Chuandian region possess
315 the same extremely low attenuation structure. The Sichuan Basin belongs to an ancient craton
316 and should have a relatively thick lithosphere, whereas Tengchong Volcano should have a
317 relatively thin lithospheric thickness due to the underlying hot mantle (Sun et al., 2013; Deng &
318 Tesauro, 2016). It is generally believed that a low velocity (Lei et al., 2009), high attenuation
319 (Byrnes et al., 2019), and low effective elastic thickness (Chen et al., 2013) correspond to a thin
320 lithosphere, whereas a high velocity, low attenuation, and high effective elastic thickness
321 correspond to a thick lithosphere. However, the lithospheric thickness in this region remains
322 unresolved. Although a few traditional receiver function methods have been used to determine
323 the LAB depth distribution (Zhang et al., 2010; Hu et al., 2011; Zhang et al., 2018) in this region,
324 the results are hard to reproduce because they have quite different values, which may be due to
325 artificial interference, even though they follow a similar pattern. Therefore, a robust and

quantitative analysis of the lithospheric thickness in this region is of great significance for understanding its tectonic evolution.

4.1 GC_SRF-based data processing approach

The analyzed teleseismic S waveform data were collected from 60 permanent stations between 86°–111°E and 22°–96°N (Figure 9) during the January 2010–December 2015 period (Zheng et al., 2010). We selected teleseismic S waveforms from Ms ≥ 5.5 earthquakes that occurred at epicentral distances of 50°–90° and possessed SNR_H greater than 5 for the GC_SRF approach. We obtained 18239 SRFs with clear Sp phases from 879 seismic events after the preprocessing steps (see Methods section) and deconvolution.

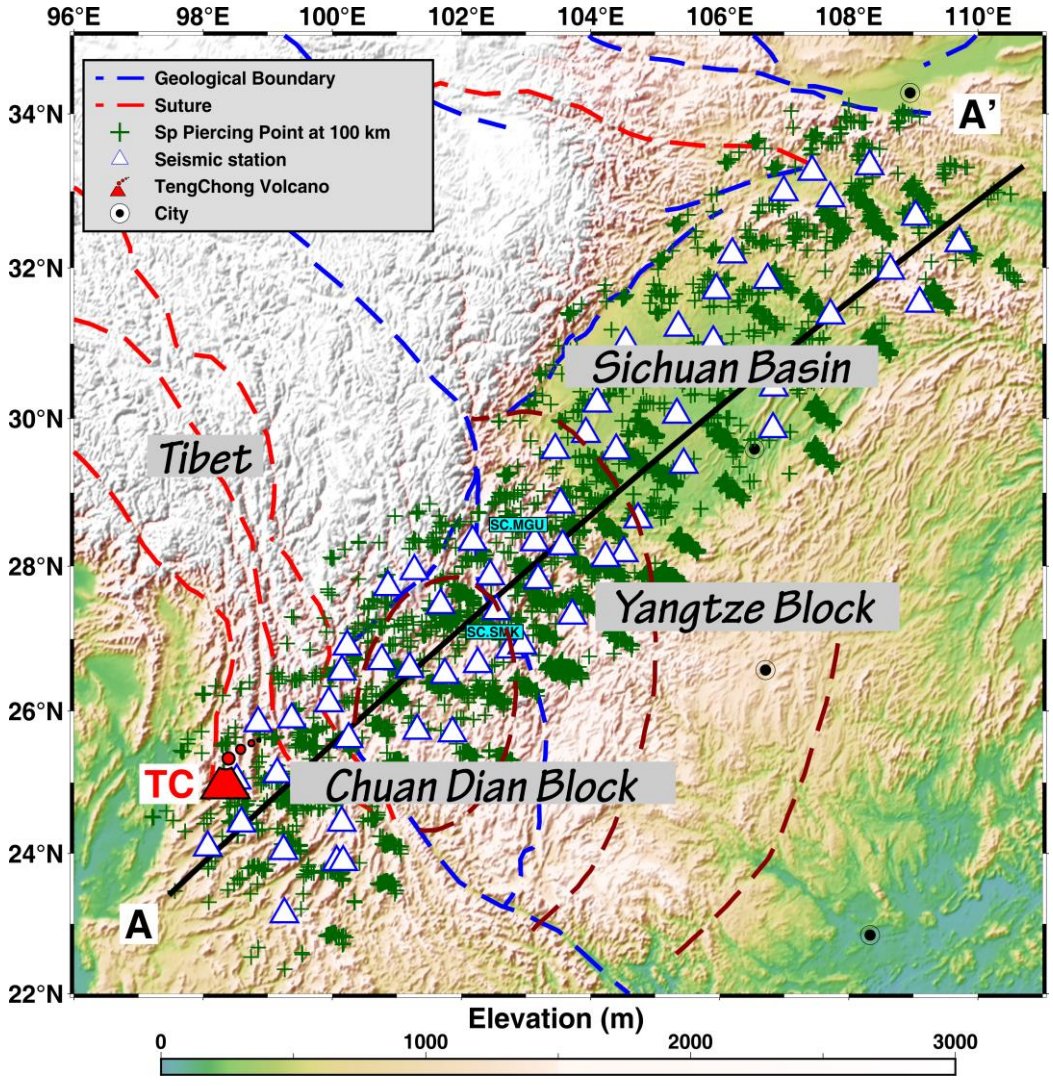

Figure 9: Topography of southeastern Tibet and adjacent regions. White triangles with blue lines represent the 59 stations used in this study. The black solid line represents the location of the migration profile A-A'. Dark-green crosses mark the piercing points of the corresponding SRFs at 100 km. Blue dashed lines mark geological boundaries. Red dashed lines represent suture belts. Dark red circular lines outline the inner, middle, and outer zones of the Permian Emeishan Large Igneous Province. Abbreviations: TC, Tengchong Volcano.

We then reversed the time axis and performed RMSE reordering, followed by CCP stacking and migration. Different RMSE percentages (5%–100%) were tested in our estimations, with an example from station SC.MGU shown in Figure 10. Figure 10a and 10b show the SRFs before and after RMSE reordering, respectively, Figure 10c shows the change in RMSE with index number, and Figure 10d and 10e show the stacked waveforms for different RMSE percentages. These two latter figures show that the RMSE percentage directly affects the amplitudes of both the Smp and SLp phases. Previous studies (Farra & Vinnik, 2000; Hansen et al., 2009; Abt et al., 2010) have indicated that a consistent and robust Smp phase can be considered the premise for discussing the SLp phase. After comparing other percentages, the selection of 30% ensures that the SLp seismic phase can be significantly distinguished under the condition that the Smp phase is as clear as possible. We finally chose the SRF dataset with a 30% RMSE percentage for the CCP stacking and migration steps to ensure the reliability of the stacked waveform.

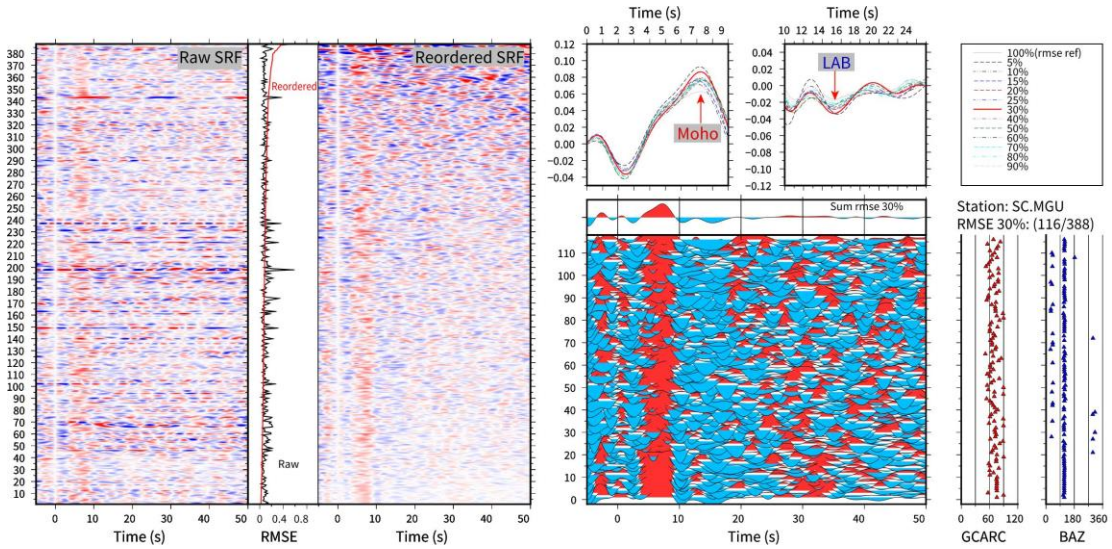

Figure 10: The reordered SRFs based on RMSE at station SC.MGU. (a) Raw SRFs after deconvolution. (b) the RMSE values corresponding to each SRF. The black line shows the RMSE of the raw sequence, while the red for reordered ones. (c) reordered SRFs based on RMSE. (d) and (e) present the Smp phase and SLp phase corresponding to different RMSE percentages. (f) SRFs of 30% RMSE percentage, and the top waveform indicates with the summation of these waveforms. The epicentral distance (GCARC) and back-azimuth (BAZ) for each event as well as the total number of SRFs are listed in (g) and (h).

4.2 Post-stack migration results in southeastern Tibet

Post-stack migration is performed in the same way as that in the 2-D synthetic test. A modified 1-D IASP91 velocity model that is based on the adjacent crustal structure (Yao, 2020) was used to calculate the delay times and piercing points and perform the frequency-domain wavefield extrapolation. We separately selected 0.03 Hz and 0.05 Hz as the lower cutoff frequency limits (Zhang et al., 2018; Zhang et al., 2019) and 0.2 Hz and 0.25 Hz as the upper cutoff frequency limits to reduce the noise and illuminate the LAB depths.

The most prominent features in the CCP cross-section are the positive Moho phases (red-filled seismic waveforms in Figure 11a) at approximately 5–8 s, which can be continuously traced along the section. There are discontinuous negative phases (cyan-filled waveforms in Figure 11a) between approximately 10 and 25 s under the shallow positive Moho phase conversions. The post-stack migration results for different frequency contents, 0.03–0.2 Hz (Figure 11b), 0.03–0.25 Hz (Figure 11c), and 0.05–0.25 Hz (Figure 11d), possess discontinuity patterns that are similar to those in the CCP image (Figure 11a). The discontinuous negative (blue) layer exhibits larger variations at depth than the overlying continuous positive (red) layer.

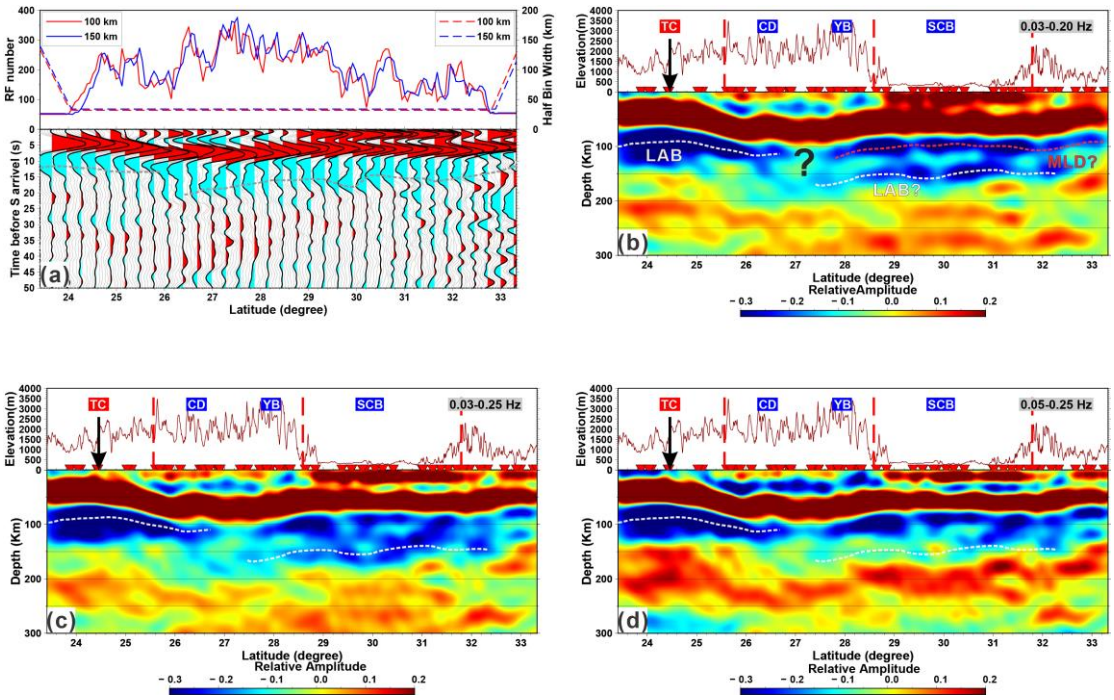

Figure 11: Common conversion point (CCP) stacking profile and post-stack migration image profile along A-A' shown in Figure 7. (a) Stacked sections of S (0.03–0.5 Hz) receiver functions after moveout corrected to epicentral distance of 0. The coherent negative SLp phase is traced by gray dashed lines. The Top panel presents the RF number and half width for each bin. (b-d) post-stack migration SRF images. Different frequency contributions of the data were considered in imaging: (b)0.03-0.2Hz; (c) 0.03-0.25Hz; (d) 0.05-0.25Hz. On each top panel, the red solid lines show the topography, and the red dashed lines represent geological boundaries. The white dashed lines on the bottom panel of (b-d) indicate LAB while the red dashed line in (b) presents the possible mid-lithospheric discontinuities (MLDs).

4.3 Geodynamic implications of the lithospheric structure

It is known that the SLp phase is usually submerged in the Smp sidelobe, as discussed in previous studies (Li et al., 2007; Kumar et al., 2012; Shen et al., 2019; Kind et al., 2020). We evaluated the robustness of the Moho and LAB depths using the criteria proposed by Zhang et al. (2018); we only discuss the primary characteristics in this section. We carefully determined the negative phase that is adjacent to the Moho as the LAB signal, which is traced by the dashed gray line in Figure 11a. However, whether the negative phase between Moho and LAB can be interpreted as a mid-lithospheric discontinuity (MLD), such as the MLD observation beneath the

North China Craton (Chen et al., 2014; Sun & Kennett, 2017), is a key issue that we plan to address in future research. We prefer to interpret the shallow visible strong negative phase below Moho under the Sichuan Basin as an MLD based on previous and recent lithospheric thickness results at Tengchong Volcano (Huang et al., 2002; Lei et al., 2009; Zhang et al., 2015) and the Sichuan Basin (Zhang et al., 2010; Chen et al., 2013; Huang et al., 2014).

The mid-crustal positive velocity gradient (PVG) is widely interpreted to be the result of thick sediment cover, as observed in other basins (Li et al., 2007; Chen et al., 2009; Mohsen et al., 2011; Tao et al., 2014). Recent research has suggested that the sediment cover across the Sichuan Basin ranges from 6 to 13 km in thickness (Xia et al., 2021). Our results indicate a discontinuous distribution pattern of the PVG that is concentrated mainly in the Sichuan Basin area. It is interesting that the spatial distribution range of the PVG is consistent with the range of low elevations within the basin area; we therefore interpret the PVG to represent the basement of the Sichuan Basin sediments.

A thick crust lies beneath the Sichuan Basin (~50 km), whereas a thin crust lies beneath Tengchong Volcano (~40 km), with the thickest crust observed in the Chuandian region (~60 km; Figure 11b). This pattern is consistent with comprehensive geophysical investigations that revealed magmatic underplating beneath the Chuandian region (Xu et al., 2014; Chen et al., 2015; Deng et al., 2016), even though the SRF uncertainties are larger than the uncertainties associated with the PRF and active seismic results. Furthermore, our study highlights a lithospheric thickness of ~160 km beneath the Sichuan Basin, with a thickness of ~90 km beneath Tengchong Volcano. The discontinuity patterns of the crust and lithosphere are consistent with previous SRF studies (Hu et al., 2011; Peng et al., 2021) in the same region; however, our results are obtained without any artificial interference. Previous studies have employed receiver function, ambient noise tomography, and body-wave and surface-wave tomography methods to clarify both the Moho discontinuities and LAB near our study region (Zhou et al., 2012; Wang et al., 2021; Wei et al., 2022), with each of these studies suggesting a thin crust and thin lithosphere beneath Tengchong Volcano. A thick (150–180 km) lithosphere that underlies a crustal lid (35–50 km) that has also been observed beneath the Sichuan Basin (Zhang et al., 2010; Wang et al., 2018; Zhang et al., 2018), with the thick lithosphere beneath the basin being a typical characteristic of this ancient craton (Li et al., 2021; Xu et al., 2021).

However, the LAB beneath the Chuandian region is not clear compared with that of Sichuan basin and Tengchong Volcano. Permian Emeishan flood basalts have been emplaced beneath the Chuandian region, with the lack of a detectable LAB aligning directly beneath the inner zones of the Permian Emeishan Large Igneous Province. The mantle plume model is a popular approach for explaining the geophysical and geochemical observations (Xu et al., 2007; Chen et al., 2015; Deng et al., 2016; Li et al., 2021) in large igneous provinces. The plume head could undergo strong changes and erode the overlying lithosphere owing to high temperatures and push it upward, with this being a common type of lithospheric thinning caused by a rising plume (Burov et al., 2007; Hawkesworth et al., 2017); this phenomenon is known as plume-induced lithospheric destruction. However, the lithosphere could undergo downgrowth through cooling, as demonstrated in North America (Yuan & Romanowicz, 2010; Hawkesworth et al., 2017). A recent study has also shown that the plume could also recratonize the lithosphere, mainly through compositional changes, as demonstrated in Arctic Canada (Liu et al., 2021). This newly generated LAB possesses a smaller velocity jump than the old LAB, such that its amplitude is smaller than that beneath the Sichuan Basin. We therefore suggest that the unclear LAB beneath the Chuandian region indicates regrowth of the modified lithosphere owing to mantle plume processes, which in turn produced the unique seismic velocity pattern, low attenuation, and high resistivity in this region (Li et al., 2020; Deng et al., 2021).

5. Conclusion

We proposed a new strategy, the GC_SRF strategy, to obtain the lithospheric thickness without artificial interference. We precisely determined the parameters in obtaining SRFs and avoided possible artifacts by employing grid search and correlation analysis. The 30% RMSE is employed to do the quality control. The synthetic tests indicate that this GC_SRF strategy can obtain reliable SRFs from full wavefield seismograms. Our application of the GC_SRF strategy in southeastern Tibet demonstrates this strategy yields excellent statistical consistency in single-station analysis. The migrated image shows that the Chuandian region possesses the thickest crust in the study area, followed by the Sichuan Basin, with the thinnest crust located beneath Tengchong Volcano. Furthermore, a thick lithosphere beneath the Sichuan Basin (~160 km) and a thin lithosphere beneath Tengchong Volcano (~90 km) have been clearly imaged. Another notable finding is that the LAB signal is unclear beneath the Chuandian region, which is

interpreted to indicate lithospheric regrowth after modification of the Emeishan mantle plume. These combined results suggest that this new strategy is suitable for obtaining SRFs and constraining the lithospheric thickness without artificial interference. This strategy can be widely applied to other regions for obtaining the lithospheric thickness and advancing our understanding of lithospheric evolution. The influences of different velocity jumps on the SRF amplitude warrant future research.

Data availability

We are grateful to the Data Management Centre of China National Seismic Network at Institute of Geophysics, China Earth-quake Administration (SEISDMC) for providing us with the original seismic data used in this study. The SRFs obtained for this paper can be accessed at https://doi.org/10.6084/m9.figshare.19316576.

Acknowledgments

We thank Professor Vinnik L.P, Xiaohui Yuan, Qingju Wu, Qimin Liu, Qiang Xu for valuable discussions. We appreciate Zhuo Xiao, Junliu Suwen, and the colleagues at office 724A in GIGCAS for their help and advice. This work was funded by National Science Foundation of China (41874106, 42021002), and Youth Innovation Promotion Association CAS (YIPA2018035). Some figures were plotted with matplotlib (Hunter, 2007) and Generic Mapping Tools (Wessel & Smith, 1995; Wessel et al., 2019)

References

Abt, D. L., Fischer, K. M., French, S. W., Ford, H. A., Yuan, H., &Romanowicz, B. (2010), North American lithospheric discontinuity structure imaged by Ps and Sp receiver functions, *Journal of Geophysical Research-Solid Earth*, *115*, B09301. https://doi.org/10.1029/2009JB006914.

Bijwaard, H., &Spakman, W. (2000), Non-linear global P-wave tomography by iterated linearized inversion, *Geophysical Journal International*, *141*(1), 71-82. https://doi.org/10.1046/j.1365-246X.2000.00053.x.

484 Buck, W. (1991), Modes of continental lithospheric extension, *Journal of Geophysical Research-*
485 *Solid Earth*, *96*(B12), 20161-20178. https://doi.org/10.1029/91JB01485.
486 Burov, E., Guillou-Frottier, L., d'Acremont, E., Le Pourhiet, L., &Cloetingh, S. (2007), Plume
487 head-lithosphere interactions near intra-continental plate boundaries, *Tectonophysics*, *434*(1-
488 4), 15-38. https://doi.org/10.1016/j.tecto.2007.01.002.
489 Byrnes, J. S., Bezada, M., Long, M. D., &Benoit, M. H. (2019), Thin lithosphere beneath the
490 central Appalachian Mountains: Constraints from seismic attenuation beneath the MAGIC
491 array, *Earth and Planetary Science Letters*, *519*, 297-307.
492 https://doi.org/10.1016/j.epsl.2019.04.045.
493 Chen, B., Chen, C., Kaban, M. K., Du, J., Liang, Q., &Thomas, M. (2013), Variations of the
494 effective elastic thickness over China and surroundings and their relation to the lithosphere
495 dynamics, *Earth and Planetary Science Letters*, *363*, 61-72.
496 https://doi.org/10.1016/j.epsl.2012.12.022.
497 Chen, L. (2009), Lithospheric structure variations between the eastern and central North China
498 Craton from S- and P-receiver function migration, *Physics of the Earth and Planetary*
499 *Interiors*, *173*(3-4), 216-227. https://doi.org/10.1016/j.pepi.2008.11.011.
500 Chen, L., Cheng, C., &Wei, Z. G. (2009), Seismic evidence for significant lateral variations in
501 lithospheric thickness beneath the central and western North China Craton, *Earth and*
502 *Planetary Science Letters*, *286*(1-2), 171-183. https://doi.org/10.1016/j.epsl.2009.06.022.
503 Chen, L., Jiang, M., Yang, J., Wei, Z., Liu, C., &Ling, Y. (2014), Presence of an
504 intralithospheric discontinuity in the central and western North China Craton: Implications
505 for destruction of the craton, *Geology*, *42*(3), 223-226. https://doi.org/10.1130/G35010.1.
506 Chen, L., Wen, L., &Zheng, T. (2005a), A wave equation migration method for receiver function
507 imaging: 1. Theory, *Journal of Geophysical Research-Solid Earth*, *110*(B11).
508 https://doi.org/10.1029/2005JB003665.
509 Chen, L., Wen, L., &Zheng, T. (2005b), A wave equation migration method for receiver function
510 imaging: 2. Application to the Japan subduction zone, *Journal of Geophysical Research-*
511 *Solid Earth*, *110*(B11). https://doi.org/10.1029/2005JB003666.
512 Chen, Y., Xu, Y., Xu, T., Si, S., Liang, X., Tian, X., et al. (2015), Magmatic underplating and
513 crustal growth in the Emeishan Large Igneous Province, SW China, revealed by a passive
514 seismic experiment, *Earth and Planetary Science Letters*, *432*, 103-114.

https://doi.org/10.1016/j.epsl.2015.09.048.

Crotwell, Philip, H., Owens, Thomas, J., Ritsema, &Jeroen (1999), The TauP Toolkit: Flexible seismic travel-time and ray-path utilities, *Seismological Research Letters*, *70*, 154--160. https://doi.org/10.1785/gssrl.70.2.154.

Deng, Y. F., &Tesauro, M. (2016), Lithospheric strength variations in Mainland China: Tectonic implications, *Tectonics*, *35*(10), 2313-2333. https://doi.org/10.1002/2016tc004272.

Deng, Y. F., Byrnes, J. S., &Bezada, M. (2021), New Insights Into the Heterogeneity of the Lithosphere-Asthenosphere System Beneath South China From Teleseismic Body-Wave Attenuation, *Geophysical Research Letters*, *48*(6). https://doi.org/10.1029/2020GL091654.

Deng, Y., Chen, Y., Wang, P., Essa, K., Xu, T., Liang, X., et al. (2016), Magmatic underplating beneath the Emeishan large igneous province (South China) revealed by the COMGRA-ELIP experiment, *Tectonophysics*, *672*, 16-23. https://doi.org/10.1016/j.tecto.2016.01.039.

Farra, V., &Vinnik, L. (2000), Upper mantle stratification by P and S receiver functions, *Geophysical Journal International*, *141*(3), 699-712. https://doi.org/10.1046/j.1365-246x.2000.00118.x.

Fischer, K. M., Ford, H. A., Abt, D. L., &Rychert, C. A. (2010), The Lithosphere-Asthenosphere Boundary, in *Annual Review of Earth and Planetary Sciences, Vol 38*, edited by R. Jeanloz and K. H. Freeman, pp. 551-575. https://doi.org/10.1146/annurev-earth-040809-152438.

Fischer, K. M., Rychert, C. A., Dalton, C. A., Miller, M. S., Beghein, C., &Schutt, D. L. (2020), A comparison of oceanic and continental mantle lithosphere, *Physics of the Earth and Planetary Interiors*, *309*. https://doi.org/10.1016/j.pepi.2020.106600.

Fu, Y. V., Gao, Y., Li, A., Li, L., &Chen, A. (2017), Lithospheric structure of the southeastern margin of the Tibetan Plateau from Rayleigh wave tomography, *Journal of Geophysical Research-Solid Earth*, *122*(6), 4631-4644. https://doi.org/10.1002/2016jb013096.

Hansen, S. E., Nyblade, A. A., Heeszel, D. S., Wiens, D. A., Shore, P., &Kanao, M. (2010), Crustal structure of the Gamburtsev Mountains, East Antarctica, from S-wave receiver functions and Rayleigh wave phase velocities, *Earth and Planetary Science Letters*, *300*(3-4), 395-401. https://doi.org/10.1016/j.epsl.2010.10.022.

Hansen, S. E., Nyblade, A. A., Julia, J., Dirks, P. H. G. M., &Durrheim, R. J. (2009), Upper-mantle low-velocity zone structure beneath the Kaapvaal craton from S-wave receiver functions, *Geophysical Journal International*, *178*(2), 1021-1027.

https://doi.org/10.1111/j.1365-246X.2009.04178.x.

Haskell, N. (1962), Crustal reflection of plane P and SV waves, *Journal of Geophysical Research*, *67*(12), 4751-+. https://doi.org/10.1029/JZ067i012p04751.

Hawkesworth, C. J., Cawood, P. A., Dhuime, B., &Kemp, T. I. S. (2017), Earth's Continental Lithosphere Through Time, in *Annual Review of Earth and Planetary Sciences, Vol 45*, edited by R. Jeanloz and K. H. Freeman, pp. 169-198. https://doi.org/10.1146/annurev-earth-063016-020525.

Hopper, E., &Fischer, K. (2015), The meaning of midlithospheric discontinuities: A case study in the northern US craton, *Geochemistry Geophysics Geosystems*, *16*(12), 4057-4083. https://doi.org/10.1002/2015GC006030.

Houseman, G. A., Mckenzie, D. P., &Molnar, P. (1981), Convective Instability of a Thickened Boundary-Layer and Its Relevance for the Thermal Evolution of Continental Convergent Belts, *Journal of Geophysical Research*, *86*(Nb7), 6115-6132. https://doi.org/10.1029/JB086iB07p06115.

Hu, J., Xu, X., Yang, H., Wen, L., &Li, G. (2011), S receiver function analysis of the crustal and lithospheric structures beneath eastern Tibet, *Earth and Planetary Science Letters*, *306*(1-2), 77-85. https://doi.org/10.1016/j.epsl.2011.03.034.

Huang, J. L., Zhao, D. P., &Zheng, S. H. (2002), Lithospheric structure and its relationship to seismic and volcanic activity in southwest China, *Journal of Geophysical Research-Solid Earth*, *107*(B10). https://doi.org/10.1029/2000jb000137.

Huang, M.-H., Buergmann, R., &Freed, A. M. (2014), Probing the lithospheric rheology across the eastern margin of the Tibetan Plateau, *Earth and Planetary Science Letters*, *396*, 88-96. https://doi.org/10.1016/j.epsl.2014.04.003.

Huang, Z., Wang, L., Xu, M., Zhao, D., Mi, N., &Yu, D. (2019), P and S Wave Tomography Beneath the SE Tibetan Plateau: Evidence for Lithospheric Delamination, *Journal of Geophysical Research-Solid Earth*, *124*(10), 10292-10308. https://doi.org/10.1029/2019jb017430.

Huang, Z.-X., Li, H.-Y., &Xu, Y. (2013), Lithospheric S-wave velocity structure of the North-South Seismic Belt of China from surface wave tomography, *Chinese Journal of Geophysics*, *56*(4), 1121-1131. (In Chinese with English abstract) https://doi.org/10.6038/cjg20130408.

Hunter, J. D. (2007), Matplotlib: A 2D graphics environment, *Computing in Science &*

Engineering, *9*(3), 90-95. https://doi.org/10.1109/mcse.2007.55.

Kawakatsu, H., Kumar, P., Takei, Y., Shinohara, M., Kanazawa, T., Araki, E., et al. (2009), Seismic Evidence for Sharp Lithosphere-Asthenosphere Boundaries of Oceanic Plates, *Science*, *324*(5926), 499-502. https://doi.org/10.1126/science.1169499.

Kennett, B., &Engdahl, E. (1991), Traveltimes for global earthquake location and phase identification, *Geophysical Journal International*, *105*(2), 429-465. https://doi.org/10.1111/j.1365-246X.1991.tb06724.x.

Kind, R., Mooney, W. D., &Yuan, X. (2020), New insights into the structural elements of the upper mantle beneath the contiguous United States from S-to-P converted seismic waves, *Geophysical Journal International*, *222*(1), 646-659. https://doi.org/10.1093/gji/ggaa203.

Kind, R., Yuan, X., &Kumar, P. (2012), Seismic receiver functions and the lithosphere-asthenosphere boundary, *Tectonophysics*, *536*, 25-43. https://doi.org/10.1016/j.tecto.2012.03.005.

Kumar, P., Kind, R., &Yuan, X. (2010), Receiver function summation without deconvolution, *Geophysical Journal International*, *180*(3), 1223-1230. https://doi.org/10.1111/j.1365-246X.2009.04469.x.

Kumar, P., Kind, R., Yuan, X., &Mechie, J. (2012), USArray Receiver Function Images of the Lithosphere-Asthenosphere Boundary, *Seismological Research Letters*, *83*(3), 486-491. https://doi.org/10.1785/gssrl.83.3.486.

Kumar, P., Yuan, X., Kind, R., &Ni, J. (2006), Imaging the colliding Indian and Asian lithospheric plates beneath Tibet, *Journal of Geophysical Research-Solid Earth*, *111*(B6). https://doi.org/10.1029/2005jb003930.

Langston, C. A. (1979), STRUCTURE UNDER MOUNT RAINIER, WASHINGTON, INFERRED FROM TELESEISMIC BODY WAVES, *Journal of Geophysical Research*, *84*(NB9), 4749-4762. https://doi.org/10.1029/JB084iB09p04749.

Lei, J., &Zhao, D. (2016), Teleseismic P-wave tomography and mantle dynamics beneath Eastern Tibet, *Geochemistry Geophysics Geosystems*, *17*(5), 1861-1884. https://doi.org/10.1002/2016gc006262.

Lei, J., Li, Y., Xie, F., Teng, J., Zhang, G., Sun, C., et al. (2014), Pn anisotropic tomography and dynamics under eastern Tibetan plateau, *Journal of Geophysical Research-Solid Earth*, *119*(3), 2174-2198. https://doi.org/10.1002/2013jb010847.

608 Lei, J., Zhao, D., &Su, Y. (2009), Insight into the origin of the Tengchong intraplate volcano and
609 seismotectonics in southwest China from local and teleseismic data, *Journal of Geophysical*
610 *Research-Solid Earth*, *114*. https://doi.org/10.1029/2008jb005881.
611 Levinson, N. (1946), The Wiener Rms (Root Mean Square) Error Criterion in Filter Design and
612 Prediction, *Journal of Mathematics and Physics*, *25*(4), 261-278.
613 https://doi.org/10.1002/sapm1946251261.
614 Li, W., Chen, Y., Liang, X., &Xu, Y.-G. (2021), Lateral Seismic Anisotropy Variations Record
615 Interaction Between Tibetan Mantle Flow and Plume-Strengthened Yangtze Craton, *Journal*
616 *of Geophysical Research-Solid Earth*, *126*(4). https://doi.org/10.1029/2020jb020841.
617 Li, X., Ma, X. B., Chen, Y., Xue, S., Varentsov, I. M., &Bai, D. H. (2020), A plume-modified
618 lithospheric barrier to the southeastward flow of partially molten Tibetan crust inferred from
619 magnetotelluric data, *Earth and Planetary Science Letters*, *548*.
620 https://doi.org/10.1016/j.epsl.2020.116493.
621 Li, X., Yuan, X., &Kind, R. (2007), The lithosphere-asthenosphere boundary beneath the
622 western United States, *Geophysical Journal International*, *170*(2), 700-710.
623 https://doi.org/10.1111/j.1365-246X.2007.03428.x.
624 Ligorria, J., &Ammon, C. (1999), Iterative deconvolution and receiver-function estimation,
625 *Bulletin of the Seismological Society of America*, *89*(5), 1395-1400.
626 https://doi.org/10.1785/BSSA0890051395.
627 Liu, L., Klemperer, S. L., &Blanchette, A. R. (2021), Western Gondwana imaged by S receiver-
628 functions (SRF): New results on Moho, MLD (mid-lithospheric discontinuity) and LAB
629 (lithosphere-asthenosphere boundary), *Gondwana Research*, *96*, 206-218.
630 https://doi.org/10.1016/j.gr.2021.04.009.
631 Liu, X., &Zhao, D. (2021), Seismic evidence for a plume-modified oceanic lithosphere-
632 asthenosphere system beneath Cape Verde, *Geophysical Journal International*, *225*(2), 872-
633 886. https://doi.org/10.1093/gji/ggab012.
634 Mohsen, A., Asch, G., Mechie, J., Kind, R., Hofstetter, R., Weber, M., et al. (2011), Crustal
635 structure of the Dead Sea Basin (DSB) from a receiver function analysis, *Geophysical*
636 *Journal International*, *184*(1), 463-476. https://doi.org/10.1111/j.1365-246X.2010.04853.x.
637 Mojaver, O. B., Darbyshire, F., &Dave, R. (2021), Lithospheric Structure and Flat-Slab
638 Subduction in the Northern Appalachians: Evidence From Rayleigh Wave Tomography,

Journal of Geophysical Research-Solid Earth, *126*(4). https://doi.org/10.1029/2020jb020924.

Molnar, P., &Tapponnier, P. (1975), Cenozoic Tectonics of Asia: Effects of a Continental Collision: Features of recent continental tectonics in Asia can be interpreted as results of the India-Eurasia collision, *Science*, *189*(4201), 419-426. https://doi.org/10.1126/science.189.4201.419.

Niu, F. L., &Kawakatsu, H. (1996), Complex structure of mantle discontinuities at the tip of the subducting slab beneath Northeast China - A preliminary investigation of broadband receiver functions, *Journal of Physics of the Earth*, *44*(6), 701-711. https://doi.org/10.4294/jpe1952.44.701.

Oppenheim, A. (1969), Speech analysis-synthesis system based on homomorphic filtering, *Journal of the Acoustical Society of America*, *45*(2), 458-+. https://doi.org/10.1121/1.1911395.

Peng, H., Badal, J., Hu, J., Yang, H., &Liu, B. (2021), Lithospheric dynamics in the vicinity of the Tengchong volcanic field (southeastern margin of Tibet): an investigation using P receiver functions, *Geophysical Journal International*, *224*(2), 1327-1344. https://doi.org/10.1093/gji/ggaa517.

Randall, G. (1989), Efficient Calculation of Differential Seismograms for Lithospheric Receiver Functions, *Geophysical Journal International*, *99*(3), 469-481. https://doi.org/10.1111/j.1365-246X.1989.tb02033.x.

Rawlinson, N., &Fishwick, S. (2012), Seismic structure of the southeast Australian lithosphere from surface and body wave tomography, *Tectonophysics*, *572*, 111-122. https://doi.org/10.1016/j.tecto.2011.11.016.

Reading, A., Kennett, B., &Sambridge, M. (2003), Improved inversion for seismic structure using transformed, S-wavevector receiver functions: Removing the effect of the free surface, *Geophysical Research Letters*, *30*(19). https://doi.org/10.1029/2003GL018090.

Ritsema, J., van Heijst, H., &Woodhouse, J. (2004), Global transition zone tomography, *Journal of Geophysical Research-Solid Earth*, *109*(B2). https://doi.org/10.1029/2003JB002610.

Ritzwoller, M., Shapiro, N., Barmin, M., &Levshin, A. (2002), Global surface wave diffraction tomography, *Journal of Geophysical Research-Solid Earth*, *107*(B12). https://doi.org/10.1029/2002JB001777.

Robinson, E., &Treitel, S. (1976), Net downgoing energy and resulting minimum-phase property

of downgoing waves, *Geophysics*, *41*(6), 1394-1396. https://doi.org/10.1190/1.1440689.

Robinson, E., &Treitel, S. (2000), *Geophysical signal analysis*, Society of Exploration Geophysicists. https://doi.org/10.1190/1.9781560802327.

Rost, S., &Thomas, C. (2002), Array seismology: Methods and applications, *Reviews of Geophysics*, *40*(3). https://doi.org/10.1029/2000rg000100.

Shen, X., Kim, Y., Song, T.-R. A., &Lim, H. (2019), Data-oriented constraint on the interpretation of S receiver function and its application to observations of seismic discontinuities in the lithosphere-asthenosphere system, *Geophysical Journal International*, *219*(1), 496-513. https://doi.org/10.1093/gji/ggz316.

Stammler, K. (1993), Seismichandler programmable multichannel data handler for interactive and automatic processing of seismological analyses, *Computers & Geosciences*, *19*(2), 135-140. https://doi.org/10.1016/0098-3004(93)90110-Q.

Sun, W., &Kennett, B. (2017), Mid-lithosphere discontinuities beneath the western and central North China Craton, *Geophysical Research Letters*, *44*(3), 1302-1310. https://doi.org/10.1002/2016GL071840.

Sun, Y. J., Dong, S. W., Zhang, H., Li, H., &Shi, Y. L. (2013), 3D thermal structure of the continental lithosphere beneath China and adjacent regions, *Journal of Asian Earth Sciences*, *62*, 697-704. https://doi.org/10.1016/j.jseaes.2012.11.020.

Tao, K., Niu, F., Ning, J., Chen, Y. J., Grand, S., Kawakatsu, H., et al. (2014), Crustal structure beneath NE China imaged by NECESSArray receiver function data, *Earth and Planetary Science Letters*, *398*, 48-57. https://doi.org/10.1016/j.epsl.2014.04.043.

Tapponnier, P., Peltzer, G., Ledain, A., Armijo, R., &Cobbold, P. (1982), Propagating extrusion tectonics in asia - new insights from simple experiments with plasticine, *Geology*, *10*(12), 611-616. https://doi.org/10.1130/0091-7613(1982)10<611:PETIAN>2.0.CO;2.

Thybo, H. (2006), The heterogeneous upper mantle low velocity zone, *Tectonophysics*, *416*(1-4), 53-79. https://doi.org/10.1016/j.tecto.2005.11.021.

Thybo, H., Bulut, N., Grund, M., Mauerberger, A., Makushkina, A., Artemieva, I. M., et al. (2021), ScanArray-A Broadband Seismological Experiment in the Baltic Shield, *Seismological Research Letters*, *92*(5), 2811-2823. https://doi.org/10.1785/0220210015.

Treitel, S., &Robinson, E. A. (1966), Design of high-resolution of digital filters, *IEEE Transactions on Geoscience Electronics*, *GE 4*(1), 25-&.

https://doi.org/10.1109/TGE.1966.271203.

Ulrych, T. J., Somerville, P. G., Jensen, O. G., &Ellis, R. M. (1972), Homomorphic Deconvolution of Some Teleseismic Events, *Bulletin of the Seismological Society of America*, *62*(5), 1269-+. https://doi.org/10.1785/BSSA0620051269.

Vinnik, L. P., Chenet, H., Gagnepain-Beyneix, J., &Lognonne, P. (2001), First seismic receiver functions on the Moon, *Geophysical Research Letters*, *28*(15), 3031-3034. https://doi.org/10.1029/2001gl012859.

Vinnik, L. P., Reigber, C., Aleshin, I. M., Kosarev, G. L., Kaban, M. K., Oreshin, S. I., et al. (2004), Receiver function tomography of the central Tien Shan, *Earth and Planetary Science Letters*, *225*(1-2), 131-146. https://doi.org/10.1016/j.epsl.2004.05.039.

Wang, R. J. (1999), A simple orthonormalization method for stable and efficient computation of Green's functions, *Bulletin of the Seismological Society of America*, *89*(3), 733-741. https://doi.org/10.1785/BSSA0890030733.

Wang, W., Wu, J., &Hammond, J. O. S. (2021), Mantle Dynamics Beneath the Sichuan Basin and Eastern Tibet From Teleseismic Tomography, *Tectonics*, *40*(2). https://doi.org/10.1029/2020tc006319.

Wang, X., Chen, L., Ai, Y., Xu, T., Jiang, M., Ling, Y., et al. (2018), Crustal structure and deformation beneath eastern and northeastern Tibet revealed by P-wave receiver functions, *Earth and Planetary Science Letters*, *497*, 69-79. https://doi.org/10.1016/j.epsl.2018.06.007.

Wei, Y., Zhang, S., Li, M., Wu, T., Hua, Y., Zhang, Y., et al. (2022), Regional lithospheric deformation beneath the East Qinling-Dabie orogenic belt based on ambient noise tomography, *Geophysical Journal International*, *228*(2), 1294-1312. https://doi.org/10.1093/gji/ggab393.

Wessel, P., &Smith, W. H. F. (1995), New version of the generic mapping tools, *Eos, Transactions American Geophysical Union*, *76*(33), 329-329. https://doi.org/10.1029/95EO00198.

Wessel, P., Luis, J. F., Uieda, L., Scharroo, R., Wobbe, F., Smith, W. H. F., et al. (2019), The Generic Mapping Tools Version 6, *Geochemistry Geophysics Geosystems*, *20*(11), 5556-5564. https://doi.org/10.1029/2019gc008515.

Wilson, D. C., Angus, D. A., Ni, J. F., &Grand, S. P. (2006), Constraints on the interpretation of S-to-P receiver functions, *Geophysical Journal International*, *165*(3), 969-980.

https://doi.org/10.1111/j.1365-246X.2006.02981.x.

Wu, Q., Tian, X., Zhang, N., Li, W., &Zeng, R. (2003a), Receiver function estimated by wiener filtering, *Earthquake Research in China*, *19*(1), 41-47. (In Chinese with English abstract)

Wu, Q., Tian, X., Zhang, N., Li, W., &Zeng, R. (2003b), Receiver function estimated by maximum entropy deconvolution, *Acta Seismologica Sinica*, *25*(4), 382-389. (In Chinese with English abstract)

Xia, X., Li, Z., Bao, F., Xie, J., Shi, Y., You, Q., et al. (2021), Sedimentary structure of the Sichuan Basin derived from seismic ambient noise tomography, *Geophysical Journal International*, *225*(1), 54-67. https://doi.org/10.1093/gji/ggaa578.

Xu, Q., Pei, S. P., Yuan, X. H., Zhao, J. M., Liu, H. B., Tu, H. W., et al. (2019), Seismic Evidence for Lateral Asthenospheric Flow Beneath the Northeastern Tibetan Plateau Derived From S Receiver Functions, *Geochemistry Geophysics Geosystems*, *20*(2), 883-894. https://doi.org/10.1029/2018gc007986.

Xu, Q., Zhao, J. M., Yuan, X. H., Liu, H. B., &Pei, S. P. (2017), Detailed Configuration of the Underthrusting Indian Lithosphere Beneath Western Tibet Revealed by Receiver Function Images, *Journal of Geophysical Research-Solid Earth*, *122*(10), 8257-8269. https://doi.org/10.1002/2017jb014490.

Xu, T., Wu, Z., Zhang, Z., Tian, X., Deng, Y., Wu, C., et al. (2014), Crustal structure across the Kunlun fault from passive source seismic profiling in East Tibet, *Tectonophysics*, *627*, 98-107. https://doi.org/10.1016/j.tecto.2013.11.010.

Xu, X., Ding, Z., Shi, D., &Li, X. (2013), Receiver function analysis of crustal structure beneath the eastern Tibetan plateau, *Journal of Asian Earth Sciences*, *73*, 121-127. https://doi.org/10.1016/j.jseaes.2013.04.018.

Xu, X., Zuza, A. V., Yin, A., Lin, X., Chen, H., &Yang, S. (2021), Permian plume-strengthened Tarim lithosphere controls the Cenozoic deformation pattern of the Himalayan-Tibetan orogen, *Geology*, *49*(1), 96-100. https://doi.org/10.1130/g47961.1.

Xu, Y. G., He, B., Huang, X. L., Luo, Z. Y., Chung, S. L., Xiao, L., et al. (2007), Identification of mantle plumes in the Emeishan Large Igneous Province, *Episodes*, *30*(1), 32-42. https://doi.org/10.18814/epiiugs/2007/v30i1/005.

Yao, H. J. (2020), Building the community velocity model in the Sichuan-Yunnan region, China: Strategies and progresses, *Science China-Earth Sciences*, *63*(9), 1425-1428.

https://doi.org/10.1007/s11430-020-9645-3.

Yao, H., Beghein, C., &van der Hilst, R. D. (2008), Surface wave array tomography in SE Tibet from ambient seismic noise and two-station analysis - II. Crustal and upper-mantle structure, *Geophysical Journal International*, *173*(1), 205-219. https://doi.org/10.1111/j.1365-246X.2007.03696.x.

Ye, Z., Li, J., Gao, R., Song, X., Li, Q., Li, Y., et al. (2017), Crustal and Uppermost Mantle Structure Across the Tibet-Qinling Transition Zone in NE Tibet: Implications for Material Extrusion Beneath the Tibetan Plateau, *Geophysical Research Letters*, *44*(20), 10316-10323. https://doi.org/10.1002/2017gl075141.

Yuan, H., &Romanowicz, B. (2010), Lithospheric layering in the North American craton, *Nature*, *466*(7310), 1063–1068. https://doi.org/10.1038/nature09332.

Yuan, X. H., Kind, R., Li, X. Q., &Wang, R. J. (2006), The S receiver functions: synthetics and data example, *Geophysical Journal International*, *165*(2), 555-564. https://doi.org/10.1111/j.1365-246X.2006.02885.x.

Zhang, G., He, Y., Ai, Y., Jiang, M., Mon, C. T., Hou, G., et al. (2021), Indian continental lithosphere and related volcanism beneath Myanmar: Constraints from local earthquake tomography, *Earth and Planetary Science Letters*, *567*. https://doi.org/10.1016/j.epsl.2021.116987.

Zhang, H., Teng, J., Tian, X., Zhang, Z., Gao, R., &Liu, J. (2012), Lithospheric thickness and upper-mantle deformation beneath the NE Tibetan Plateau inferred from S receiver functions and SKS splitting measurements, *Geophysical Journal International*, *191*(3), 1285-1294. https://doi.org/10.1111/j.1365-246X.2012.05667.x.

Zhang, L., Hu, Y.L., Qin, M., Duan, Y., Duan, Y.Z., Peng, H.C., et al. (2015) Study on crustal and lithosphere thicknesses of Tengchong volcanic area in Yunnan, Chinese Journal of Geophysics, 58(5), 1622-1633. (In Chinese with English abstract) https://doi.org/10.6038/cjg20150514.

Zhang, R., Wu, Q., Sun, L., He, J., &Gao, Z. (2014), Crustal and lithospheric structure of Northeast China from S-wave receiver functions, *Earth and Planetary Science Letters*, *401*, 196-205. https://doi.org/10.1016/j.epsl.2014.06.017.

Zhang, Y. Y., Chen, L., Ai, Y. S., &Jiang, M. M. (2019), Lithospheric structure beneath the central and western North China Craton and adjacent regions from S-receiver function

imaging, *Geophysical Journal International*, *219*(1), 619-632. https://doi.org/10.1093/gji/ggz322.

Zhang, Y. Y., Chen, L., Ai, Y. S., Jiang, M. M., Xu, W. W., &Shen, Z. Y. (2018), Lithospheric structure of the South China Block from S-receiver function, *Chinese Journal of Geophysics*, *61*(1), 138-149. (In Chinese with English abstract) https://doi.org/10.6038/cjg2018L0226.

Zhang, Z., Yuan, X., Chen, Y., Tian, X., Kind, R., Li, X., et al. (2010), Seismic signature of the collision between the east Tibetan escape flow and the Sichuan Basin, *Earth and Planetary Science Letters*, *292*(3-4), 254-264. https://doi.org/10.1016/j.epsl.2010.01.046.

Zheng, X. F., Yao, Z.-X., Liang, J.-H., &Zheng, J. (2010), The Role Played and Opportunities Provided by IGP DMC of China National Seismic Network in Wenchuan Earthquake Disaster Relief and Researches, *Bulletin of the Seismological Society of America*, *100*(5B), 2866-2872. https://doi.org/10.1785/0120090257.

Zhou, L., Xie, J., Shen, W., Zheng, Y., Yang, Y., Shi, H., et al. (2012), The structure of the crust and uppermost mantle beneath South China from ambient noise and earthquake tomography, *Geophysical Journal International*, *189*(3), 1565-1583. https://doi.org/10.1111/j.1365-246X.2012.05423.x.

Figure all.

Figure 1

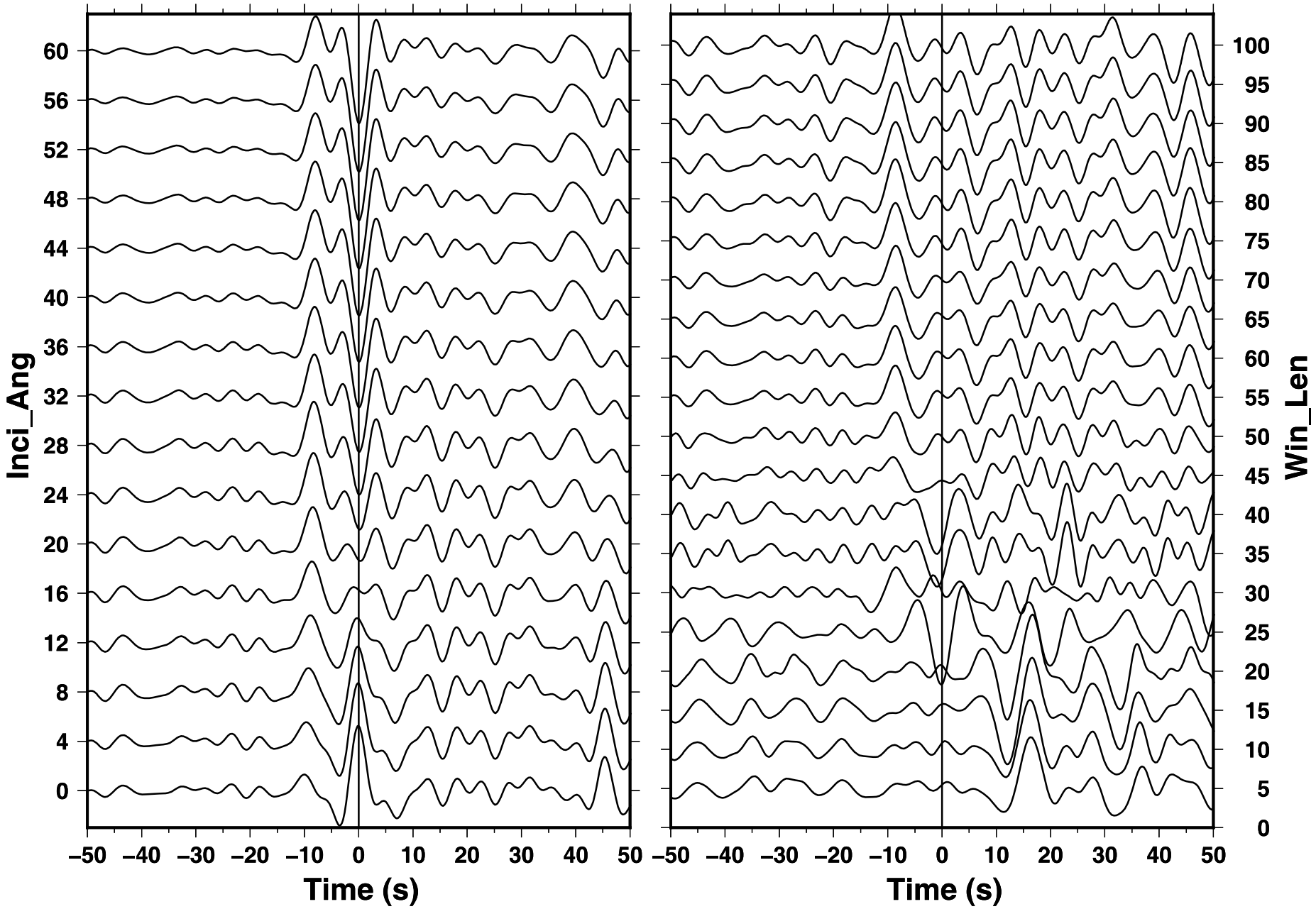
Inci_Ang
60
56
52
48
44
40
36
32
28
24
20
16
12
8
4
0
−50 −40 −30 −20 −10 0 10 20 30 40 50
Time (s)
−50 −40 −30 −20 −10 0 10 20 30 40 50
Time (s)
Win_Len
100
95
90
85
80
75
70
65
60
55
50
45
40
35
30
25
20
15
10
5
0

Figure 2

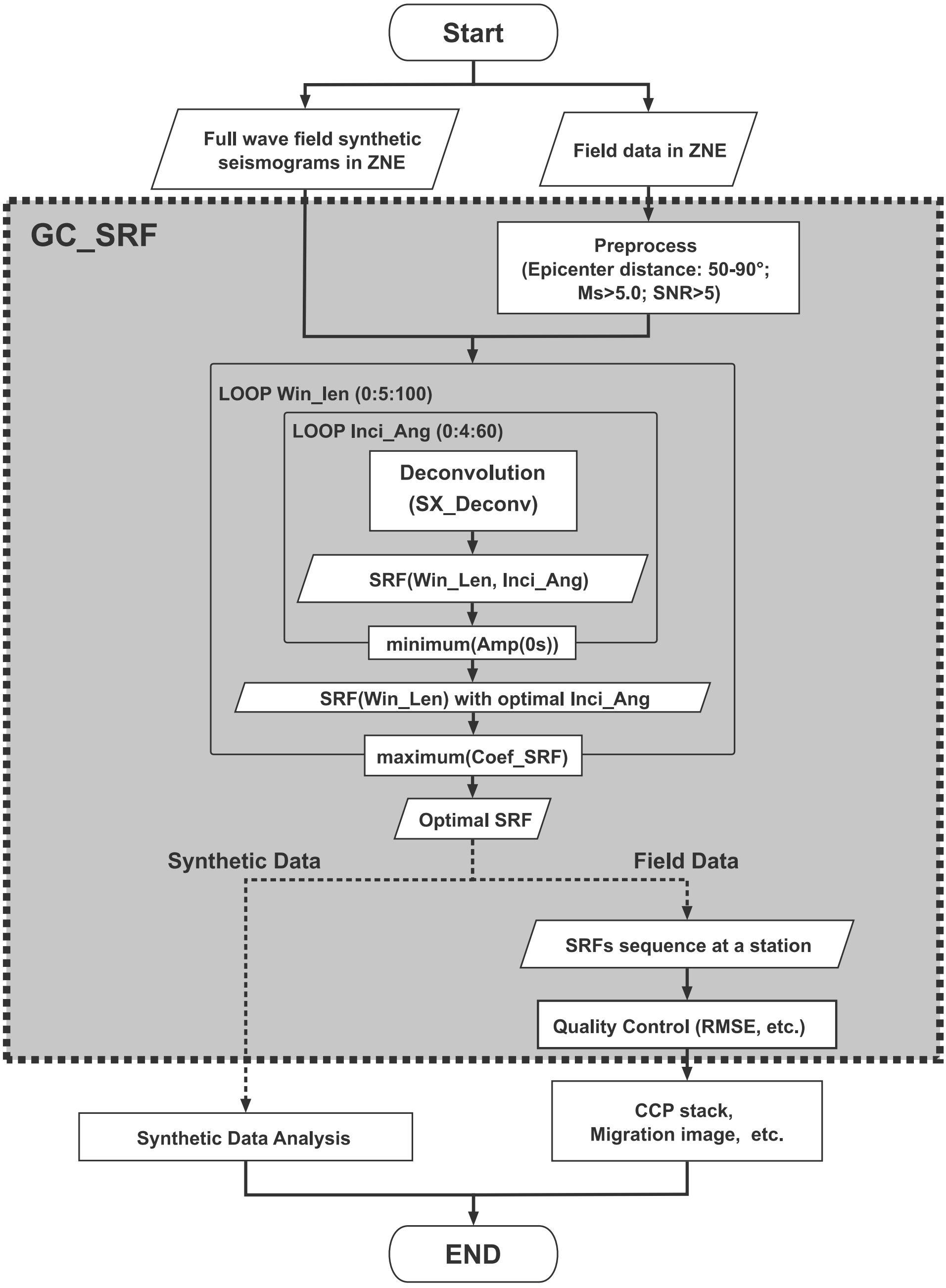
Start
Full wave field synthetic seismograms in ZNE
Field data in ZNE
GC_SRF
Preprocess
(Epicenter distance: 50-90°;
Ms>5.0; SNR>5)
LOOP Win_len (0:5:100)
LOOP Inci_Ang (0:4:60)
Deconvolution
(SX_Deconv)
SRF(Win_Len, Inci_Ang)
minimum(Amp(0s))
SRF(Win_Len) with optimal Inci_Ang
maximum(Coef_SRF)
Optimal SRF
Synthetic Data
Field Data
SRFs sequence at a station
Quality Control (RMSE, etc.)
CCP stack,
Migration image, etc.
Synthetic Data Analysis
END

Figure 3

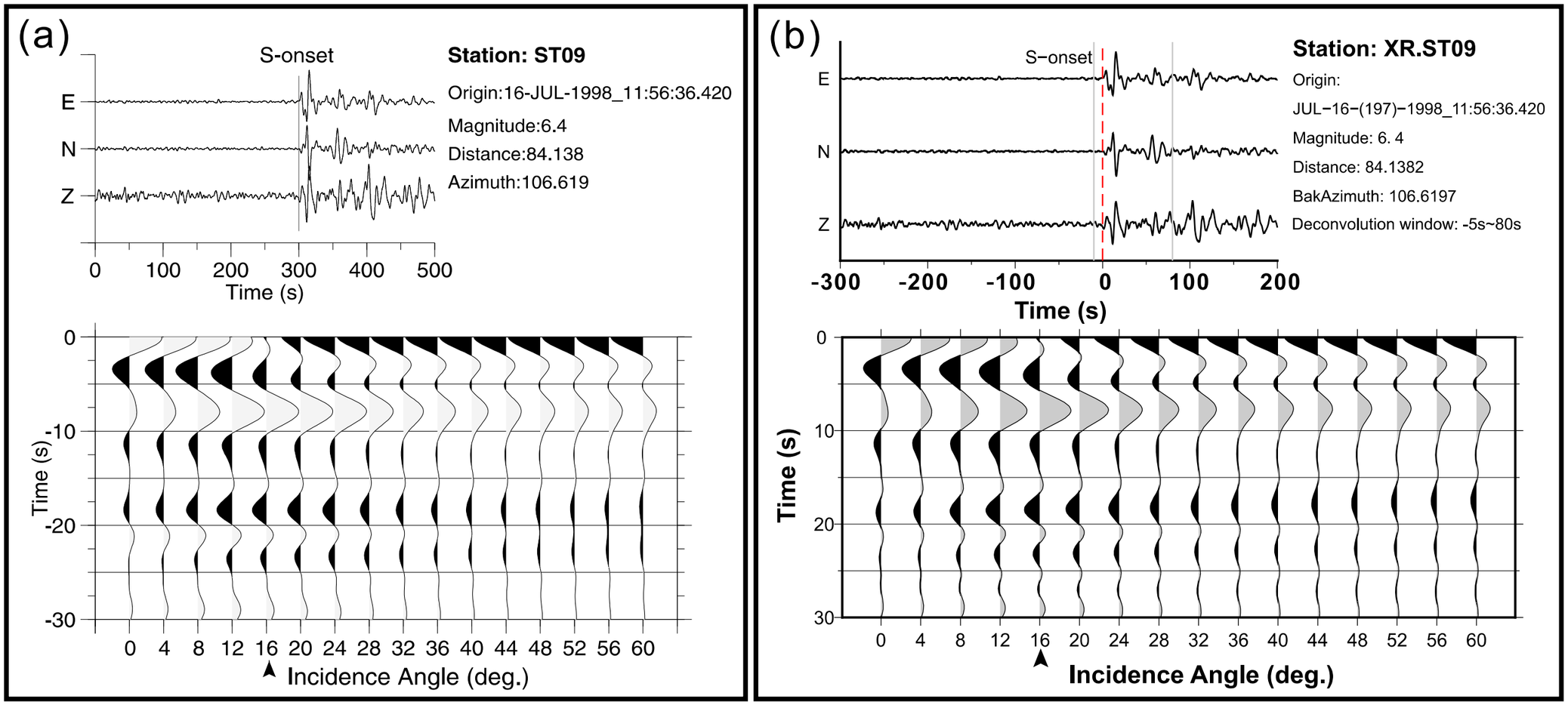
(a)
S-onset
E
N
Z
Station: ST09
Origin:16-JUL-1998_11:56:36.420
Magnitude:6.4
Distance:84.138
Azimuth:106.619
0 100 200 300 400 500
Time (s)
0 -10 -20 -30
Time (s)
0 4 8 12 16 20 24 28 32 36 40 44 48 52 56 60
Incidence Angle (deg.)
(b)
S-onset
E
N
Z
Station: XR.ST09
Origin:
JUL-16-(197)-1998_11:56:36.420
Magnitude: 6. 4
Distance: 84.1382
BakAzimuth: 106.6197
Deconvolution window: -5s~80s
-300 -200 -100 0 100 200
Time (s)
0 10 20 30
Time (s)
0 4 8 12 16 20 24 28 32 36 40 44 48 52 56 60
Incidence Angle (deg.)

Figure 4

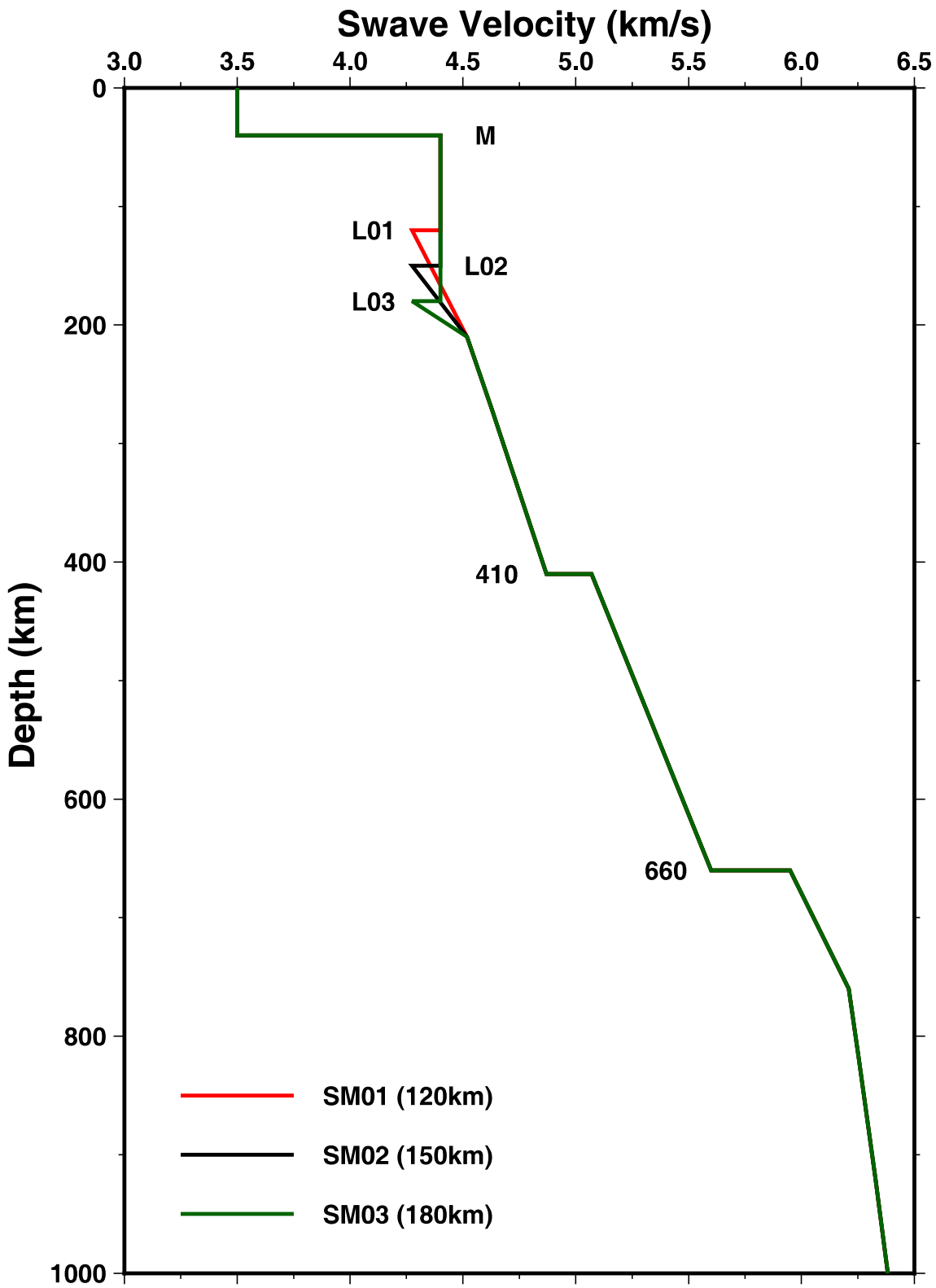
Swave Velocity (km/s)
3.0
3.5
4.0
4.5
5.0
5.5
6.0
6.5
0
200
400
600
800
1000
Depth (km)
M
L01
L02
L03
410
660
SM01 (120km)
SM02 (150km)
SM03 (180km)

Figure 5

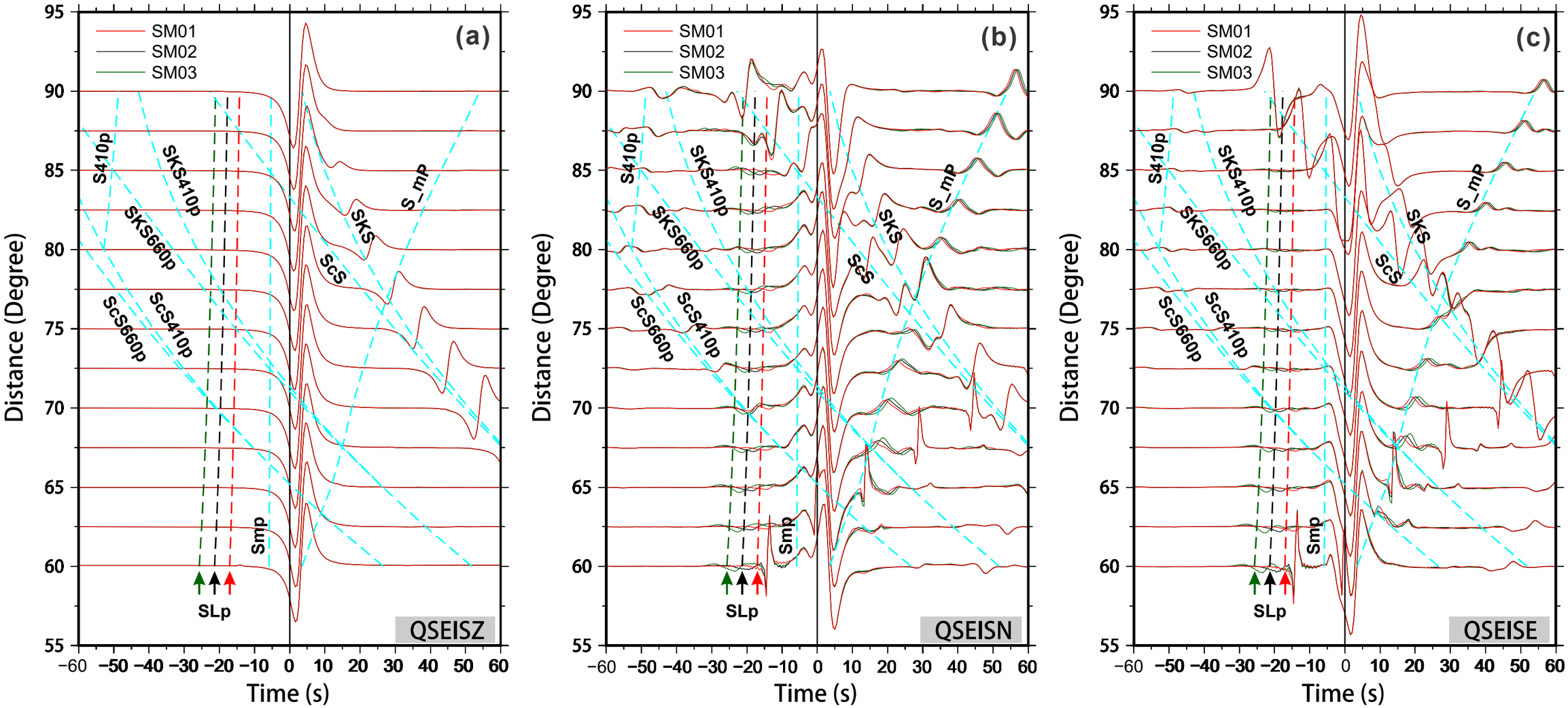
SM01
SM02
SM03
(a)
(b)
(c)
S410p
SKS410p
SKS660p
ScS660p
ScS410p
Smp
SKS
ScS
S_mP
SLp
QSEISZ
QSEISN
QSEISE
Distance (Degree)
Time (s)
95
90
85
80
75
70
65
60
55
−60 −50 −40 −30 −20 −10 0 10 20 30 40 50 60

Figure 6

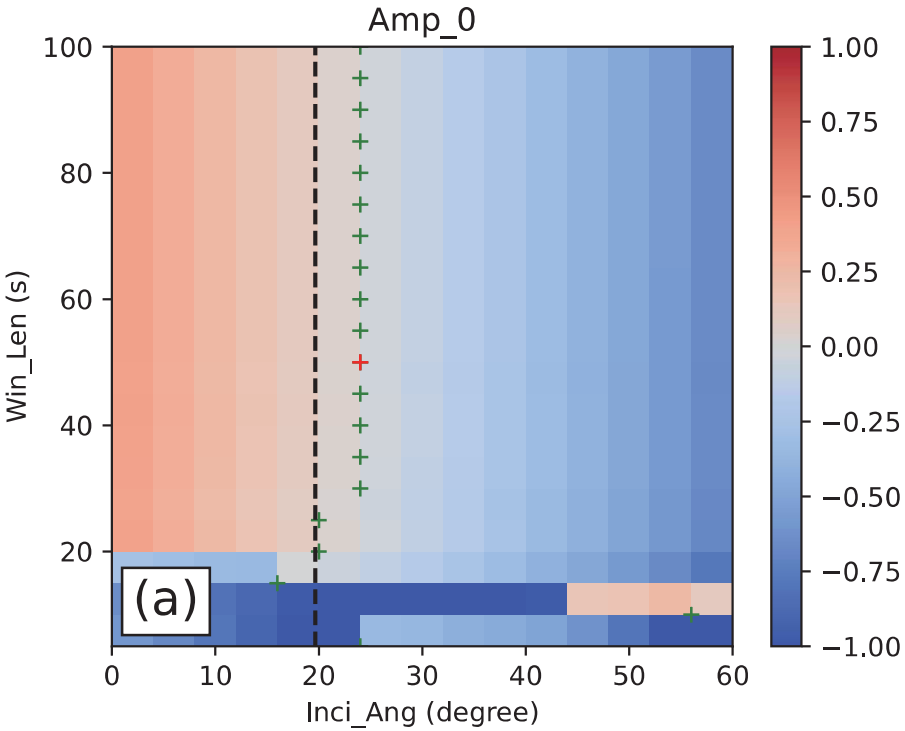
Amp_0
Win_Len (s)
Inci_Ang (degree)
(a)
1.00
0.75
0.50
0.25
0.00
−0.25
−0.50
−0.75
−1.00

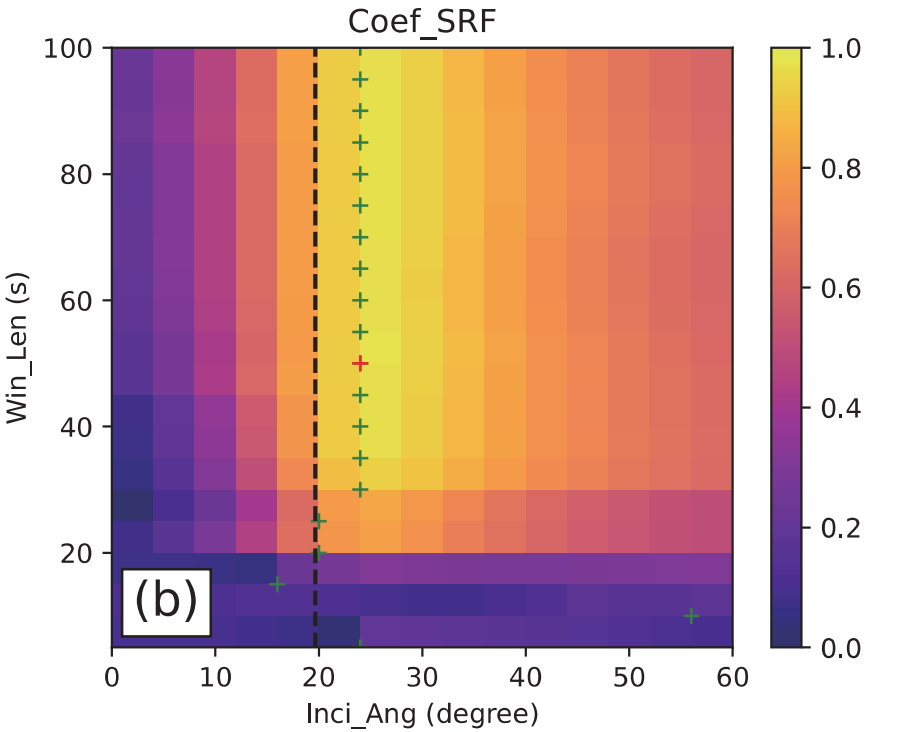
Coef_SRF
Win_Len (s)
Inci_Ang (degree)
(b)

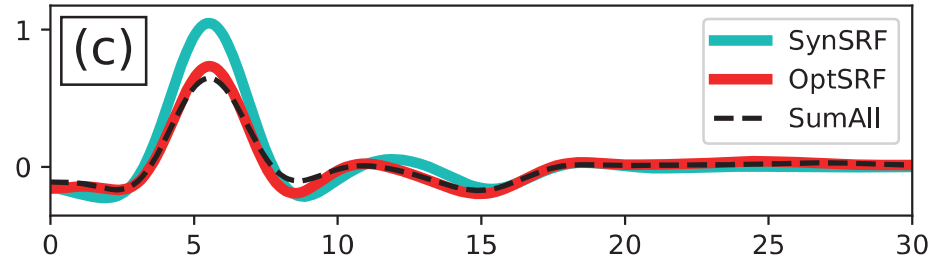
(c)
SynSRF
OptSRF
SumAll

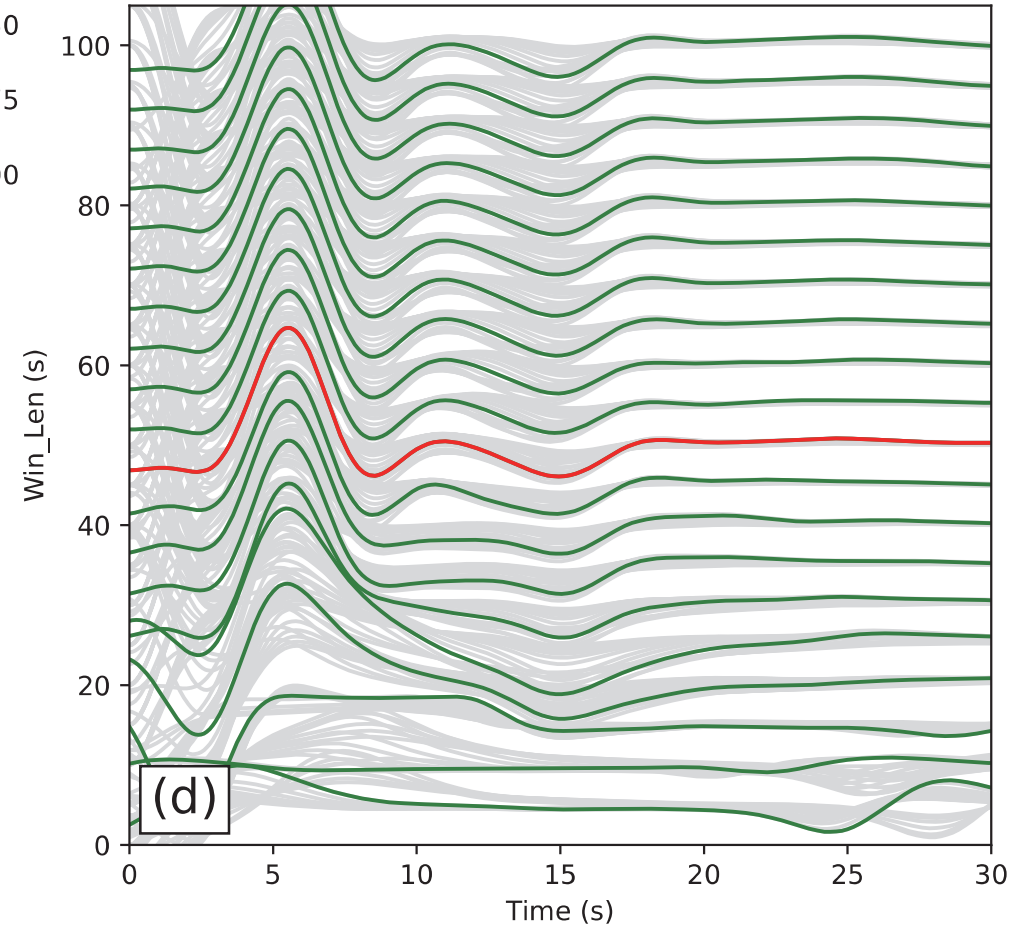
Win_Len (s)
Time (s)
(d)

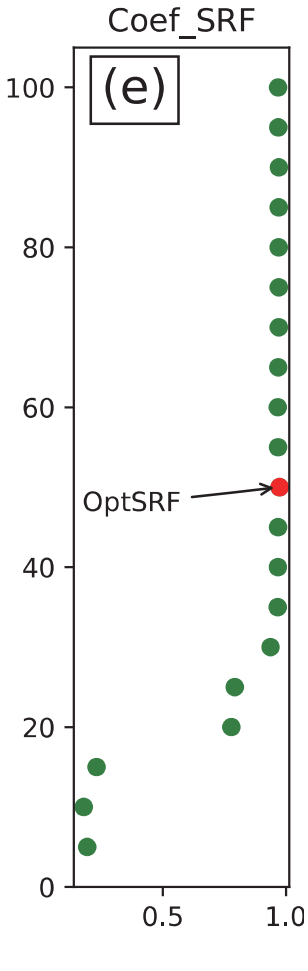
Coef_SRF
(e)
OptSRF

Figure 7

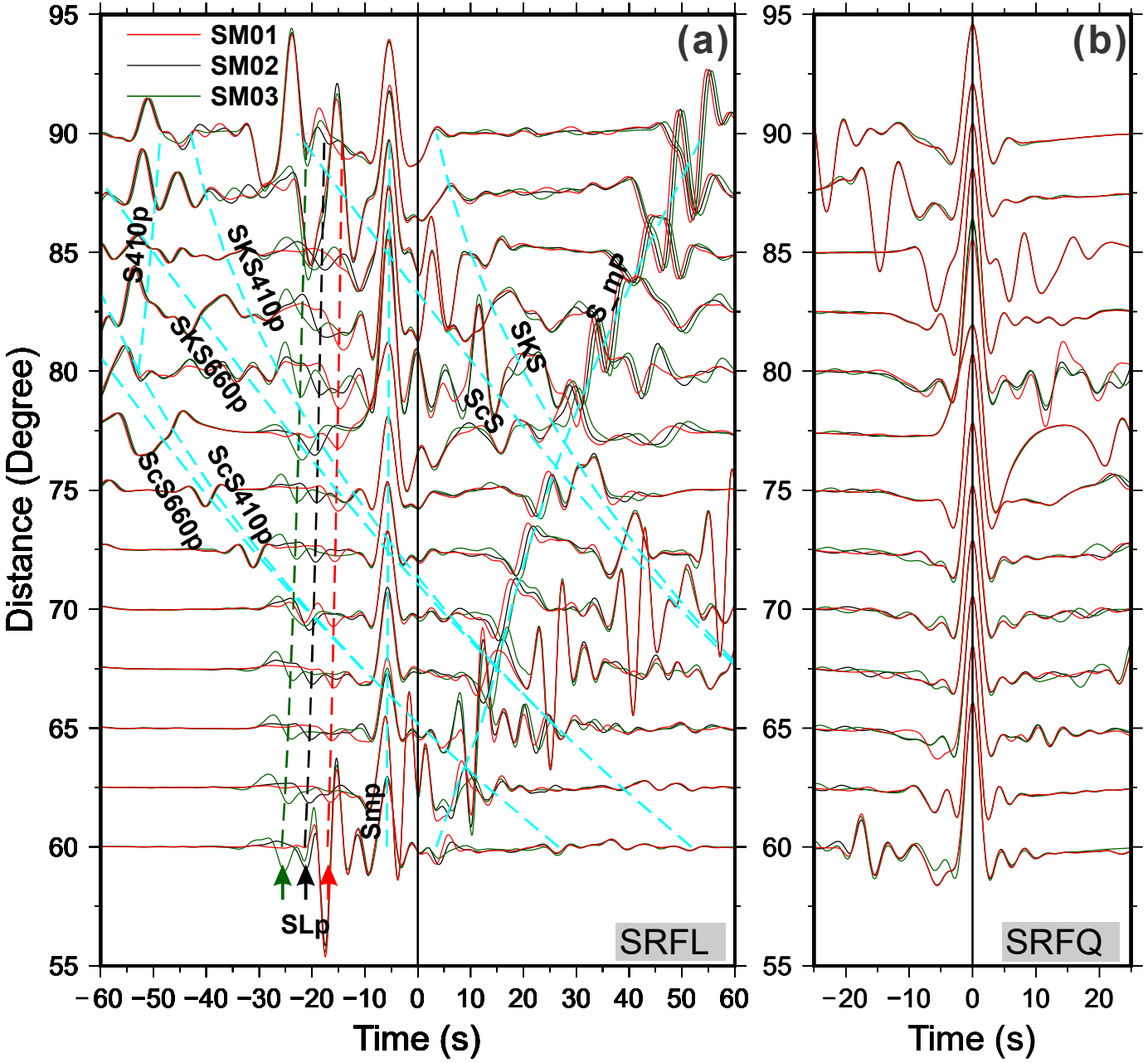
SM01
SM02
SM03
(a)
(b)
SKS
SKS410p
SKS660p
ScS
ScS410p
ScS660p
Smp
SLp
SRFL
SRFQ
Distance (Degree)
Time (s)
Time (s)

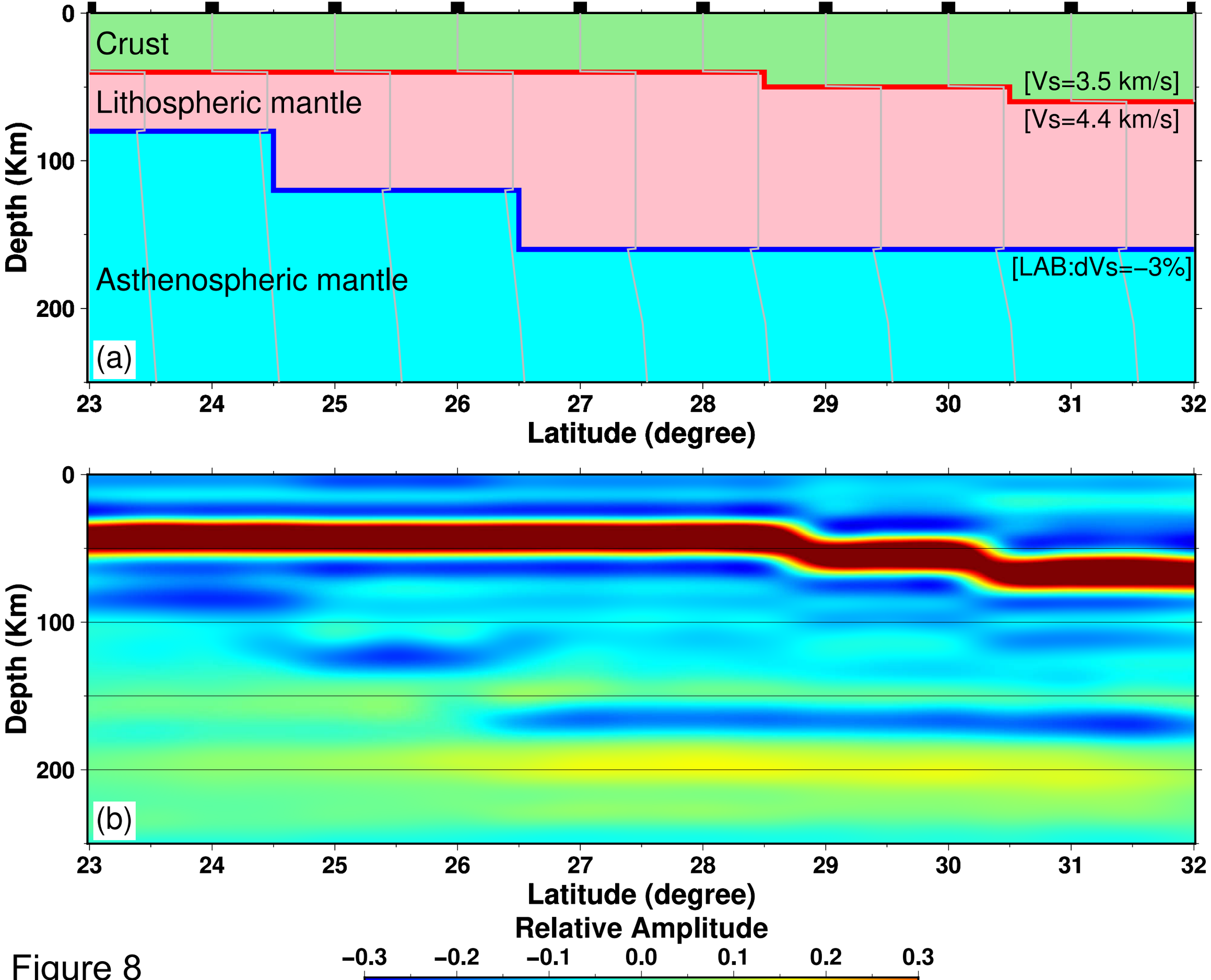
Crust
Lithospheric mantle
Asthenospheric mantle
[Vs=3.5 km/s]
[Vs=4.4 km/s]
[LAB:dVs=–3%]
(a)
(b)
Depth (Km)
0
100
200
23
24
25
26
27
28
29
30
31
32
Latitude (degree)
Relative Amplitude
–0.3
–0.2
–0.1
0.0
0.1
0.2
0.3

Figure 8

Figure 9

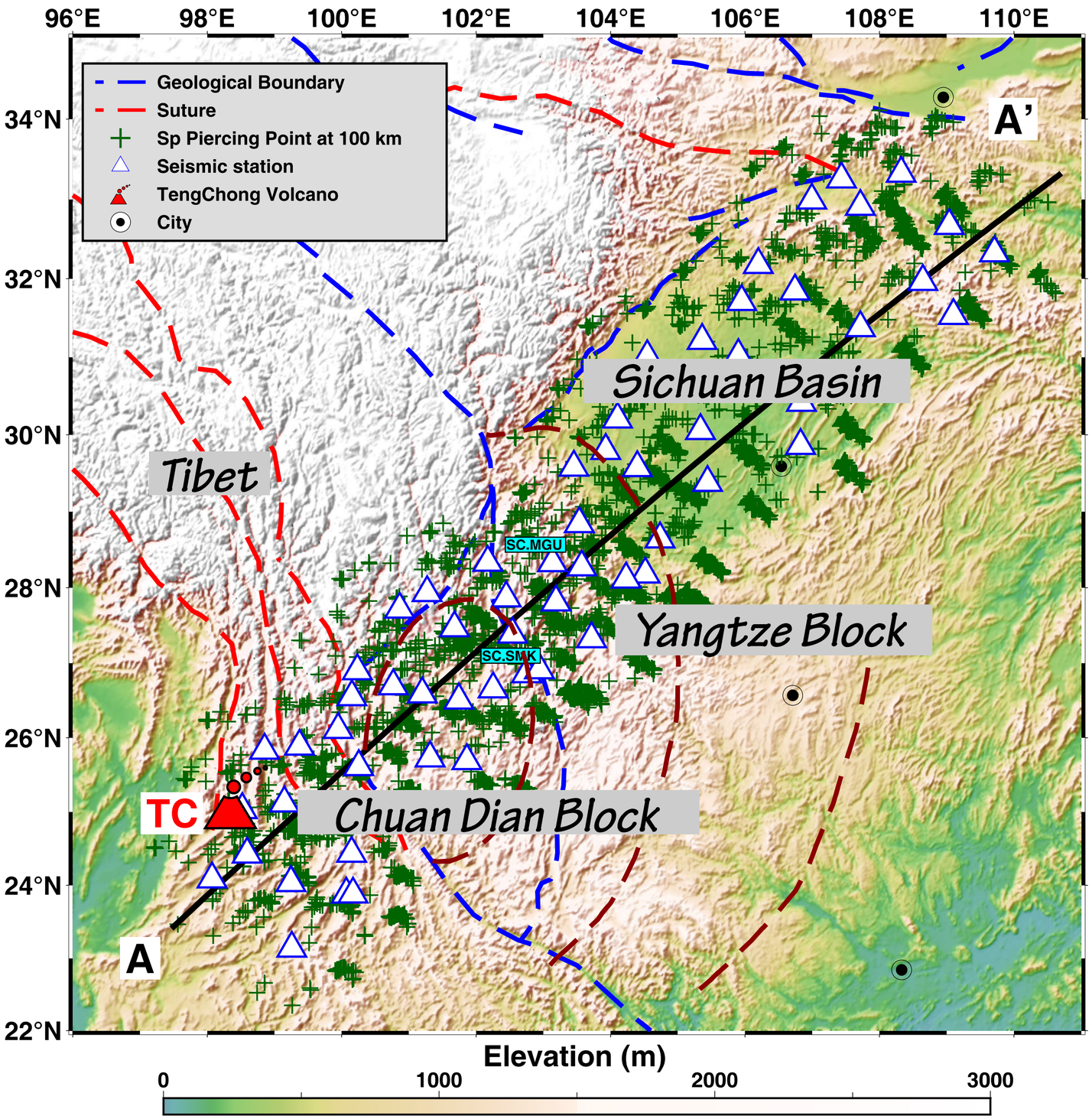
96°E
98°E
100°E
102°E
104°E
106°E
108°E
110°E
34°N
32°N
30°N
28°N
26°N
24°N
22°N
Geological Boundary
Suture
Sp Piercing Point at 100 km
Seismic station
TengChong Volcano
City
A'
A
TC
Tibet
Sichuan Basin
Yangtze Block
Chuan Dian Block
SC.MGU
SC.SMK
Elevation (m)
0
1000
2000
3000

Figure 10

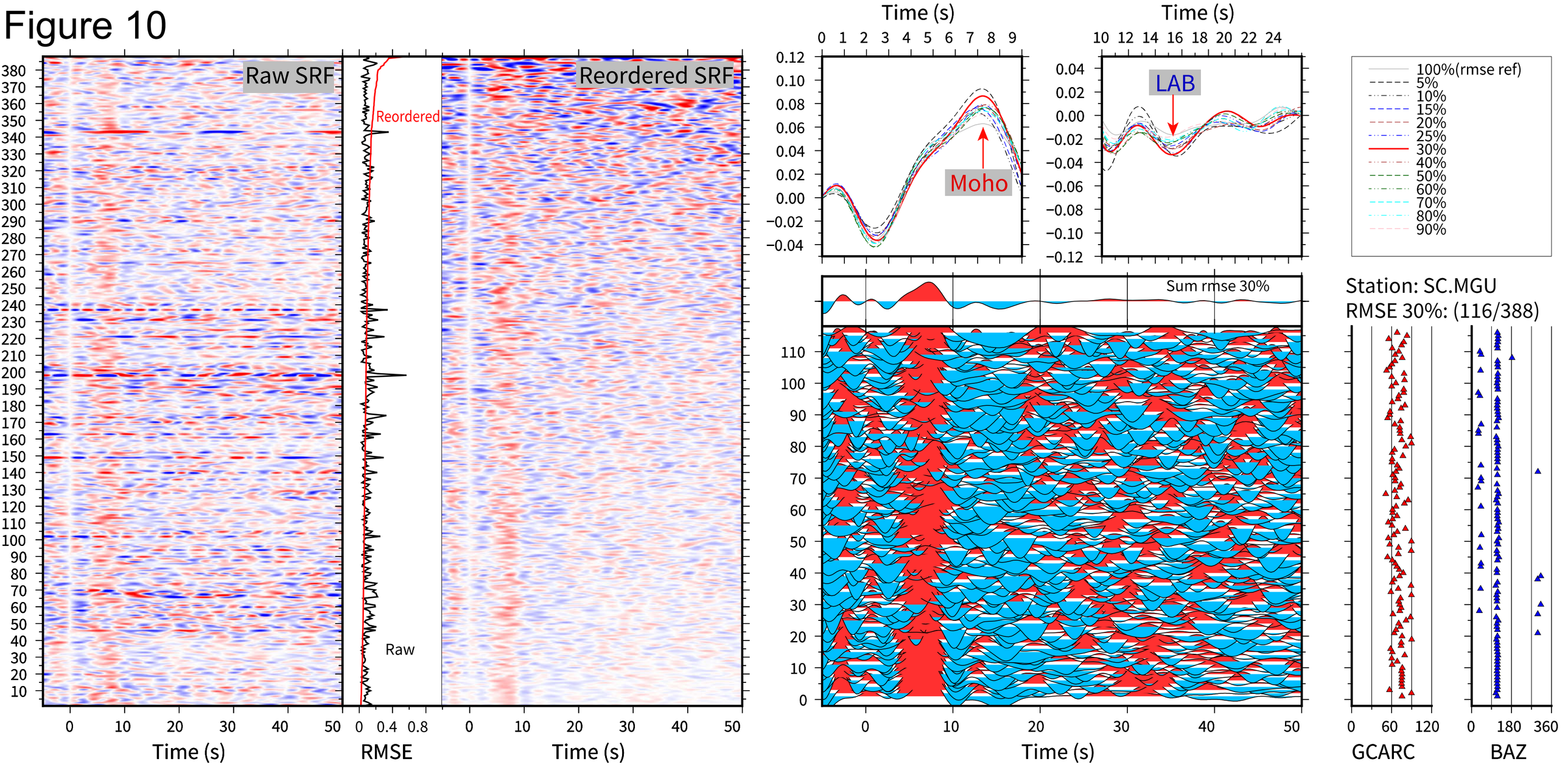
Raw SRF
Reordered SRF
Reordered
Raw
Time (s)
RMSE
Time (s)
Moho
LAB
Sum rmse 30%
100%(rmse ref)
5%
10%
15%
20%
25%
30%
40%
50%
60%
70%
80%
90%
Station: SC.MGU
RMSE 30%: (116/388)
GCARC
BAZ

Figure 11

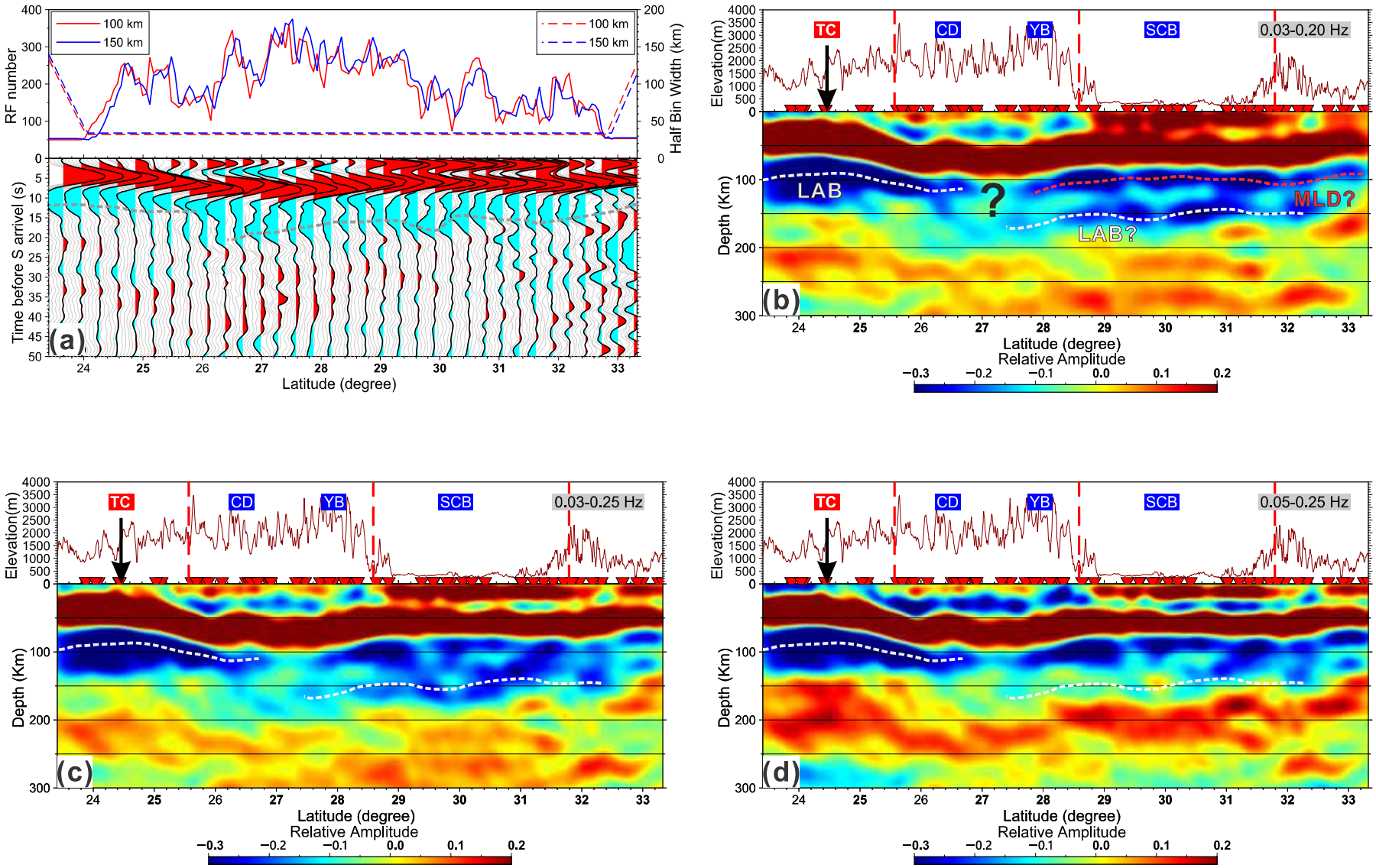
100 km
150 km
RF number
Half Bin Width (km)
Time before S arrivel (s)
(a)
Latitude (degree)
TC
CD
YB
SCB
0.03-0.20 Hz
Elevation(m)
Depth (Km)
LAB
?
MLD?
LAB?
(b)
Latitude (degree)
Relative Amplitude
0.03-0.25 Hz
(c)
0.05-0.25 Hz
(d)